Asynchronous Hierarchical Volt/var Control for Offshore Wind Farms

Yongjun Zhang, *Senior Member*, *IEEE*, Kanghua Zhong, Yingqi Yi, and Yang Liu, *Member*, *IEEE*

***Abstract*—Utilizing the reactive power (var) capability of wind turbines (WTs) has become the primary method for increasing var reserves in offshore wind farms. However, current methods place an unbearable burden on outdated equipment, which requires frequent communication. Catering to this problem, an asynchronous hierarchical voltage/var (volt/var) control (AHVC) method is proposed, which is constrained by the original communication capability and topology of collector grid, and embedded in a master-slave multi-agent system with an asynchronous hierarchical control scheme. The proposed AHVC method is built on the bilinear optimal power flow (Bilinear-OPF) model with a parallel alternating direction method of multipliers (ADMM) algorithm. It resolves voltage distortion issues in high-capacitance grids by ensuring more precise var targeting across the grid, then the var burden on the static synchronous compensator (STATCOM) is reduced. Additionally, the volt/var sensitivity-based Mahalanobis norm hyperparameter setting method ensures local compensation of var sources. The proposed AHVC method achieves rapid convergence and reliable performance amid typical load volatilities of WTs. Simulation results verify the significant improvement of accuracy and voltage stability, even under challenging communication conditions.**

***Index Terms*—Volt/var control, optimal power flow, multi-agent, offshore wind farm, wind turbine (WT), voltage distortion, voltage stability, alternating direction method of multipliers (ADMM).**

I. Introduction

WITH the rapid advancement of offshore wind power technology, offshore wind farms have been widely deployed along China's coastline. However, early-stage design flaws and hardware wear have reduced the adaptability and maintainability of aging wind farms, declining the economic viability. Among the various methods to enhance economic performance, capacity expansion represents one of the most effective ways to extend the lifetime of offshore wind farm projects [1]. Additionally, modern offshore wind farm projects are distinguished by higher construction density and increased installed capacity. In summary, the increased volatility in wind power output, due to additional installed capacity and wind speed variability, heightens uncertainties in the power flow distribution across the transmission network and imposes more stringent demands on local voltage stability.

Today, to maintain voltage stability at the point of common coupling (PCC) and comply with the voltage or reactive power (var) commands issued by grid operators, aging wind farms are required to increase their var reserves. In line with these operation requirements, this typically involves adding static synchronous compensators (STATCOMs) to raise the var reserve from 20% to 35% of the total capacity [2], [3], which significantly increases the construction costs and extends the return-on-investment periods. Therefore, coordinating var sources within the collector network to maximize STATCOM replacement has attracted significant research attention.

Early automatic voltage control (AVC) systems in wind farms relied on centralized control methods, typically deployed at switching stations. These stations functioned as device-level supervisors, collecting operation data from STATCOMs, on-load tap-changing transformers (OLTCs), and wind turbines (WTs). The control instructions were computed offline and then dispatched to the respective devices in real time [4], [5]. The primary objective was to balance the var output of each WT using proportional equations based on known power loss sensitivities [6], while also incorporating optimal power flow (OPF) for voltage/var (volt/var) optimization in wind farms [7].

However, as wind farm sizes expand, centralized control methods face the following challenges.

1) Computational complexity is posed by large-scale optimization. In these nonlinear optimization problems, the var output of WTs and their corresponding bus voltage phasors serve as decision variables. Their total number is approximately three times the number of buses, making it increasingly difficult for interior-point methods to ensure both the solution accuracy and computational efficiency when addressing this NP-hard problem. Additionally, due to the significant admittance of submarine cables, the neglect of cycle conditions leads to the nonlinear degradation of convex optimization techniques commonly used in onshore wind farms, such as semidefinite programming and second-order cone relaxation [8]. Consequently, the solution accuracy may fall be-

Manuscript received: March 4, 2025; revised: May 20, 2025; accepted: August 4, 2025. Date of CrossCheck: August 4, 2025. Date of online publication: August 22, 2025.

This work was supported in part by the Natural Science Foundation of Guangdong Province (No. 2024A1515010435) and in part by the Research and Development Program Project in Key Areas of Guangdong Province (No. 2021B0101230001).

Y. Zhang, K. Zhong, Y. Yi, and Y. Liu (corresponding author) are with the School of Electric Power, South China University of Technology, Guangzhou 510641, China (e-mail: zhangjun@scut. edu. cn; konver@foxmail. com; 827019497@qq.com; epyangliu@scut.edu.cn).

DOI: 10.35833/MPCE.2025.000141

low that of the linear or direct current (DC) models. Achieving a balance among conservatism, optimization performance, and computational cost remains a widely debated issue [9].

2) The issues of low sampling rate and diminished control accuracy present significant challenges in the context of large-scale synchronous control systems. To effectively monitor and control all WTs, AVC substations require extensive computational resources during each operation cycle. The time delay of the second-level computation from input state acquisition to output command generation, combined with the hundred-millisecond-level communication control delay in large-scale synchronous communication, is a key factor contributing to tuning errors that cause instability in feedback controllers [10]. While some studies have introduced fuzzy control and predictive control methods to mitigate time delay errors, or have incorporated WT uncertainties into multi-objective optimization to enhance robustness [11], [12], these compensatory control methods do not fundamentally reduce the inherent time delays.

Moreover, STATCOM, which serves as a redundancy control measure in this method, must not only fulfill grid voltage regulation requirements but also compensate for system-wide control errors. This places additional strains on the low-capacity STATCOMs, further increasing their operation burden.

With advancements in the semiconductor industry, the computational power of individual central processing unit (CPU) has significantly improved, making it feasible to leverage WT controllers for low-latency solutions to small-scale optimization problems. As a result, decentralized control methods have emerged as a promising alternative to addressing the above-mentioned challenges. These methods distribute global optimization tasks among independent computing agents, which exchange limited information with neighboring agents or measurement devices to generate localized computational tasks. Decentralized control methods enhance network security and, by eliminating the need for a central controller, significantly reduce the computational and communication burden on AVC substations, as well as the overall latency [13].

However, decentralized control methods also present several critical challenges that must be addressed.

1) Implicit power flow constraints complicate the decomposition of tasks. In 110 kV and above power systems with low impedance ratios, DC power flow and linear power flow algorithms exhibit significant advantages in accuracy. Due to their explicit linear structure, subtask decomposition is possible through (pseudo) inverse operations. However, in medium-voltage submarine cable systems, high impedance ratios and charging capacitances of submarine cables distort these models, making them unsuitable for real-world applications [14]. In contrast, implicit power flow constraints and convex relaxation techniques lack robust block decomposition algorithms, and parallel distributed algorithms do not provide convergence guarantees [15], [16]. As a result, these methods face computational difficulties similar to those encountered in centralized control methods.

2) The tuning of empirical hyperparameter affects the global performance of optimization. The volt/var optimal control problem in offshore wind farms is typically formulated as bi-objective optimization tasks, balancing voltage and var deviations through weighted combinations. In centralized control methods, the selection of norm coefficients has the minimal impact on the results. However, in local optimization problems, excessively low local weight ratios fail to ensure consistent directions of var outputs among WTs, leading to unnecessary long-distance var compensation. This inefficiency significantly wastes the overall var margin of wind farms.

3) Distributed algorithms and communication strategies are poorly integrated. Distributed algorithms often rely on augmented Lagrangian decomposition, using the dual ascent and the alternating direction method of multipliers (ADMM) to manage cascades in the objective and auxiliary problems. While dual ascent has demonstrated strong performance when paired with point-to-point communication strategies [17], continuous high-frequency data transmission poses a significant challenge for outdated communication devices. Potential channel congestion could lead to communication failures, reducing the robustness of optimization. Furthermore, status updates from controllers are not continuously broadcast to neighboring devices in a timely manner. This discrepancy can cause severe input mismatches in internal model controllers (IMCs) and Smith predictor controllers, potentially triggering var oscillations and voltage flicker [18].

Thus, an asynchronous hierarchical volt/var control (AHVC) method embedded in master-slave multi-agent system is proposed in this context, distinguished by its low communication dependency and high robustness to interference. Moreover, we direct considerable attention to the OPF model developed for submarine cables and the corresponding design of parallel computing algorithms. Additionally, physical and algorithmic justification for hyperparameter setting is provided for the general enhancement of applicability. The specific contributions of this paper are threefold.

1) Bilinear optimal power flow (Bilinear-OPF) model with parallel ADMM algorithm is built. In high-capacitance grid cases, existing research works encounter voltage distortion issues after the convexification of nonlinear power flow constraints. Thus, penalty terms regarding the voltage matrix are designed to approximate vector decomposition through bilinear variables. This resulting Bilinear-OPF model resolves the degradation problem of dominant eigenvalue associated with the voltage matrix, and corrects voltage distortion. Additionally, by utilizing the characteristics of the convex subproblem in updating the variables, a parallel ADMM algorithm is designed and extended to $|n|$-block computing, providing an algorithmic foundation for the implementation of the proposed AHVC method.

2) Considering the attenuation effectiveness of var compensation with distance, a volt/var sensitivity-based Mahalanobis norm hyperparameter setting method is used in the optimization objective. This method enables the orderly var substitution between the STATCOM and local compensation by WTs, effectively addressing the issues of low convergence speed and disorganized var output directions encountered in traditional methods.

3) A master-slave multi-agent system is introduced to meet the low-cost communication retrofit requirements. Asynchronous communication between the master agent and slave agent ensures the timeliness of commands after the computation of parallel ADMM algorithm with uneven delays. Meanwhile, synchronous communication between the slave agent and the WTs is employed to ensure coordinated actions. The proposed AHVC method effectively mitigates the high demands of data throughput inherent in peer-to-peer (P2P) communication within distributed control methods, while simultaneously resolving the inefficiency characteristics of centralized methods during offline operation.

The remainder of this paper is structured as follows. Section II presents the modelling of an offshore wind farm. Section III proposes the Bilinear-OPF model with the volt/var sensitivity-based Mahalanobis norm hyperparameter setting method. Then, a customized ADMM algorithm with Karush-Kuhn-Tucker (KKT) conditions is derived. Section IV outlines the asynchronous hierarchical control scheme to formulate the proposed AHVC method, detailing the $|n|$-block subproblem handled by slave agents. Section V presents case studies and shows static and dynamic test results. Finally, Section VI concludes this paper.

II. Modelling of an Offshore Wind Farm

Offshore wind farm, a prevalent form of renewable energy generation in coastal regions, typically features a collector grid configuration, as depicted in Fig. 1. These collector grids usually adopt a radial structure, with feeder lines converging at the low-voltage buses of the offshore substations. The generated power is transmitted through an on-load tap-changing transformer and a high-voltage submarine cable to the switching station, which acts as the grid connection point.

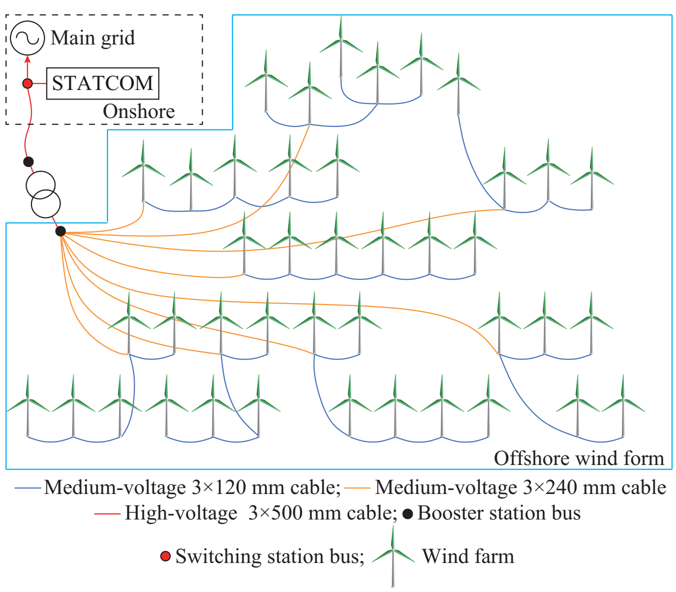

Fig. 1. Layout of offshore wind farm.

A. Collector Grid

Consider a collector grid consisting of N WTs, one offshore substation, one switching station, and an equivalent power source representing the main grid.

The buses are represented by the set $\mathcal{N} \cup \{0\}$, where $\mathcal{N} := \{1, 2, \ldots, N, \ldots, N+4\}$. The low- and high-voltage buses of the booster station are numbered $N+1$ and $N+2$, respectively; the switching station bus is numbered $N+3$; the slack bus is numbered $N+4$. The $N+3$ transmission lines in the collector grid are denoted by the set ε, and for all $\forall (i,j) \in \varepsilon$, they form an undirected graph $G = (\mathcal{N}, \varepsilon)$. The power flow in the collector grid is typically governed by the following constraints:

$$\dot{s}_j = \sum_{k:j\sim k} \dot{y}_{j,k} \dot{V}_j \left(\dot{V}_j^* - \dot{V}_k^* \right) \quad j \in \mathcal{N} \tag{1}$$

where $\dot{s}_j$ is the complex power injected into bus j by the WT; $\dot{V}_j$ is the voltage phasor at bus j; $\dot{y}_{j,k}$ is the mutual admittance between buses j and k, and typically, $\dot{y}_{j,j}$ is the self-admittance of bus j; and the superscript "*" denotes the conjugate operation. This yields a compact model as:

$$\dot{\boldsymbol{s}} = \operatorname{diag}\left(\dot{\boldsymbol{V}} \right) \dot{\boldsymbol{Y}}^* \dot{\boldsymbol{V}}^* \tag{2}$$

where $\dot{\boldsymbol{V}}, \dot{\boldsymbol{s}} \in \mathbb{C}^n$ are the voltage phasor and complex power vectors injected into the buses, respectively, and n is the total number of buses within the grid; $\operatorname{diag}(\cdot): \mathbb{C}^n \to \mathbb{C}^{n\times n}$ is the function that converts a vector into a diagonal matrix; and $\operatorname{diag}(\cdot): \mathbb{C}^{n\times n} \to \mathbb{C}^n$ is the function that extracts the diagonal elements from a matrix into a vector. The admittance matrix is symmetric and is defined as $\dot{\boldsymbol{Y}} = \boldsymbol{A}\dot{\boldsymbol{X}}_l^{-1}\boldsymbol{A}^{\mathrm{T}} + 1/2 \cdot \operatorname{diag}\left(\boldsymbol{A}\dot{\boldsymbol{Y}}_{\mathrm{GB}}\boldsymbol{A}^{\mathrm{T}} \right) \in \mathbb{C}^{|\mathcal{N}|\times|\mathcal{N}|}$, where $\boldsymbol{A} \in \mathbb{R}^{|\mathcal{N}|\times|\varepsilon|}$ is the incidence matrix, and $\dot{\boldsymbol{X}}_l \in \mathbb{C}^{|\varepsilon|}$ and $\dot{\boldsymbol{Y}}_{\mathrm{GB}} \in \mathbb{C}^{|\varepsilon|}$ are the line impedance and admittance vectors, respectively, ordered according to the branch sequence defined by $\boldsymbol{A}$.

To simplify matrix differentiation operations, we define a Hermitian matrix $\dot{\boldsymbol{W}}$:

$$\dot{\boldsymbol{W}} = \dot{\boldsymbol{V}}\dot{\boldsymbol{V}}^{\mathrm{H}} \tag{3}$$

where superscript "H" refers to the conjugate transpose operation. Equation (1) can be rewritten as:

$$\begin{cases} \dot{s}_j = \left\langle \dot{\boldsymbol{Y}}_j, \dot{\boldsymbol{W}} \right\rangle & j \in \mathcal{N} \\ rank\left(\dot{\boldsymbol{W}} \right) = 1 \end{cases} \tag{4}$$

where $\dot{\boldsymbol{Y}}_j = \boldsymbol{e}_j \boldsymbol{e}_j^{\mathrm{T}} \dot{\boldsymbol{Y}}$, and $\boldsymbol{e}_j$ is the projection vector; and the function $rank(\cdot)$ calculates the rank of the matrix. The inner product of unitary vectors $\boldsymbol{x}$ and $\boldsymbol{y}$ is defined as $\left\langle \dot{\boldsymbol{x}}, \dot{\boldsymbol{y}} \right\rangle = \left\langle \dot{\boldsymbol{y}}, \dot{\boldsymbol{x}} \right\rangle^* = \left\langle \dot{\boldsymbol{y}}^*, \dot{\boldsymbol{x}}^* \right\rangle = \dot{\boldsymbol{x}}^{\mathrm{H}}\dot{\boldsymbol{y}}$. The inner product of unitary matrices $\dot{\boldsymbol{W}}$ and $\dot{\boldsymbol{Y}}$ is similarly defined as $\left\langle \dot{\boldsymbol{Y}}, \dot{\boldsymbol{W}} \right\rangle = \left\langle \dot{\boldsymbol{W}}, \dot{\boldsymbol{Y}} \right\rangle^* = \left\langle \dot{\boldsymbol{W}}^*, \dot{\boldsymbol{Y}}^* \right\rangle = tr\left(\dot{\boldsymbol{Y}}^{\mathrm{H}}\dot{\boldsymbol{W}} \right)$, where the function $tr(\cdot): \mathbb{C}^{n\times n} \to \mathbb{C}$ calculates the trace of matrix. To preserve the linearity of operations, the power flow constraint ζ is defined by the linear operator $\mathcal{Y}(\cdot)$, such that $\zeta := \left\{ \dot{\boldsymbol{W}} \in \mathbb{C}^{n\times n} \middle| \mathcal{Y}\left(\dot{\boldsymbol{W}} \right) = \dot{\boldsymbol{s}} \right\}$. The operator $\mathcal{Y}(\cdot): \mathbb{C}^{n\times n} \to \mathbb{C}^n$ is given by the following expression:

$$\mathcal{Y}\left(\dot{\boldsymbol{W}} \right) = \left[\left\langle \dot{\boldsymbol{Y}}_1, \dot{\boldsymbol{W}} \right\rangle \ \left\langle \dot{\boldsymbol{Y}}_2, \dot{\boldsymbol{W}} \right\rangle \ \ldots \ \left\langle \dot{\boldsymbol{Y}}_n, \dot{\boldsymbol{W}} \right\rangle \right]^{\mathrm{T}} \tag{5}$$

If we define the stacking function $vec(\cdot): \mathbb{C}^{n\times n} \to \mathbb{C}^{n^2}$, the above equation can also be rewritten as:

$$\mathcal{Y}\left(\dot{\boldsymbol{W}}\right)=\dot{\boldsymbol{Y}}_{\mathrm{v}}\cdot vec\left(\dot{\boldsymbol{W}}\right) \tag{6}$$

where $\dot{\boldsymbol{Y}}_{\mathrm{v}}=\left[vec\left(\dot{\boldsymbol{Y}}_1\right),vec\left(\dot{\boldsymbol{Y}}_2\right),\dots,vec\left(\dot{\boldsymbol{Y}}_n\right)\right]^{\mathrm{T}}\in\mathbb{C}^{n\times n^2}$. The adjoint operator $\mathcal{Y}^*\left(\dot{\boldsymbol{\mu}}\right):\mathbb{C}^n\rightarrow\mathbb{C}^{n\times n}$ is defined as $\mathcal{Y}^*\left(\dot{\boldsymbol{\mu}}\right)=\sum_{j=1}^{|\mathcal{N}|}\dot{\boldsymbol{Y}}_j\dot{\mu}_j$, where $\dot{\boldsymbol{\mu}}=\left[\dot{\mu}_1,\dot{\mu}_2,\dots,\dot{\mu}_n\right]^{\mathrm{T}}$ refers to any complex vector. In an inner product space, this operator satisfies the property: $\left\langle\dot{\boldsymbol{\mu}},\mathcal{Y}\left(\dot{\boldsymbol{W}}\right)\right\rangle=\left\langle\mathcal{Y}^*\left(\dot{\boldsymbol{\mu}}\right),\dot{\boldsymbol{W}}\right\rangle$. Since this linear operator extends to the complex domain, its conjugate form must also be considered: $\bar{\mathcal{Y}}\left(\dot{\boldsymbol{W}}\right)=\dot{\boldsymbol{Y}}_{\mathrm{v}}^*\cdot vec\left(\dot{\boldsymbol{W}}\right)$ and $\bar{\mathcal{Y}}^*\left(\dot{\boldsymbol{\mu}}\right)=\sum_{j=1}^{|\mathcal{N}|}\dot{\boldsymbol{Y}}_j^*\dot{\mu}_j$. These forms satisfy $\left(\mathcal{Y}\left(\dot{\boldsymbol{W}}\right)\right)^*=\bar{\mathcal{Y}}\left(\dot{\boldsymbol{W}}^*\right)$ and $\left(\mathcal{Y}^*\left(\dot{\boldsymbol{\mu}}\right)\right)^*=\bar{\mathcal{Y}}^*\left(\dot{\boldsymbol{\mu}}^*\right)$. Moreover, $\mathcal{Y}\mathcal{Y}^*\left(\dot{\boldsymbol{\mu}}\right)=\mathcal{Y}\left(\mathcal{Y}^*\left(\dot{\boldsymbol{\mu}}\right)\right)$.

Additionally, the voltage magnitude at each bus must comply with the upper bound $V_{j,\mathrm{ub}}$ and lower bound $V_{j,\mathrm{lb}}$ of operation, while the voltage phasor of slack bus satisfies $\dot{V}_{N+3}=\left(1+\mathrm{j}0\right)$ p.u..

$$V_{j,\mathrm{lb}}\leq\left|\dot{V}_j\right|\leq V_{j,\mathrm{ub}}\quad j\in\mathcal{N} \tag{7}$$

In matrix form, we have:

$$\boldsymbol{V}_{\mathrm{lb}}^{\odot2}\leq\mathrm{diag}\left(\dot{\boldsymbol{W}}\right)\leq\boldsymbol{V}_{\mathrm{ub}}^{\odot2} \tag{8}$$

where $\boldsymbol{V}_{\mathrm{lb}},\boldsymbol{V}_{\mathrm{ub}}\in\mathbb{R}^{|\mathcal{N}|}$ are the lower and upper limits of the voltage of $|\mathcal{N}|$ buses, respectively; and $\boldsymbol{V}^{\odot2}=\boldsymbol{V}\odot\boldsymbol{V}^*$, and the operator $\odot$ refers to the Hadamard product.

B. Power Support Capability of Wind Farms

WTs operate in the maximum power point tracking (MPPT) mode, where the active power output limit is determined by the mechanical power captured from the wind. The var output fluctuates within a dynamic range. For WTs with full-scale converters, the var support capability is constrained by the capacity of the grid-side converter (GSC) [19], [20]. Typically, it does not exceed 130% of the rated capacity of WT. As a result, the buses corresponding to each turbine are modeled as PQ nodes, with power limits satisfying:

$$P_j-\mathrm{j}Q_{j,\mathrm{lb}}\leq\dot{s}_j\leq P_j+\mathrm{j}Q_{j,\mathrm{ub}}\quad j\in\{1,2,...,N\} \tag{9}$$

where $\dot{s}_j=P_j+\mathrm{j}Q_j$, and P_j and Q_j are the active and reactive power injected into bus j, respectively; and $Q_{j,\mathrm{lb}}$ and $Q_{j,\mathrm{ub}}$ are the lower and upper limits of the inductive var injection of bus j, respectively. STATCOM is a continuous volt/var regulation device with smooth adjustment capabilities. It is frequently employed to assist in the uninterrupted operation of WTs and voltage oscillation damping. STATCOMs are typically installed at the switching station, with their power limits satisfying:

$$-\mathrm{j}Q_{j,\mathrm{lb}}\leq\dot{s}_j\leq\mathrm{j}Q_{j,\mathrm{ub}}\quad j=N+2 \tag{10}$$

Given the close relationship between the var output capability of a WT and its active power output, it is necessary to perform real-time evaluation for the proposed AHVC method in this paper. For generality, we assume that all WTs operate in MPPT mode, without dead zones in the var limits.

III. Bilinear-OPF Model

This section first introduces the primal problem of static volt/var optimal control, aiming to minimize the var output and voltage deviation of STATCOM. To achieve priority control of var sources, a volt/var sensitivity-based Mahalanobis norm hyperparameter setting method is proposed. Additionally, to convexify the rank constraints without voltage distortion in the submarine cable grid, a Bilinear-OPF model is proposed along with a customized ADMM algorithm. While ensuring convexity, the algorithm updates multiple variables concurrently to accelerate the convergence.

A. Primal Problem Formulation

In most var/voltage optimization models for wind farms, the objective function is typically formulated as a weighted combination of the var margin of reactive sources and bus voltage deviations [17]. Different reactive sources or buses can be assigned Mahalanobis norm hyperparameter matrices according to their significance or regulation capabilities within the grid. This method facilitates localized var compensation and mitigates the risk of circulating var flows.

The constraints include power flow constraints, bus voltage limits, and var output limits. Thus, the primal problem for static volt/var optimal control in offshore wind farms is formulated as:

$$\left\{\begin{aligned}&\min_{\boldsymbol{W},\boldsymbol{Q}}\left(\omega_{\mathrm{q}}\left\|\boldsymbol{Q}-\boldsymbol{Q}_{\mathrm{tar}}\right\|_{\boldsymbol{K}_{\mathrm{q}}}^2+\omega_{\mathrm{v}}\left\|\mathrm{diag}\left(\dot{\boldsymbol{W}}\right)-\boldsymbol{V}_{\mathrm{tar}}^{\odot2}\right\|_{\boldsymbol{K}_{\mathrm{v}}}^2\right)\\&\text{s.t. }\ \dot{\boldsymbol{W}}\succcurlyeq0\\&\qquad rank\left(\dot{\boldsymbol{W}}\right)=1\\&\qquad \mathcal{Y}\left(\dot{\boldsymbol{W}}\right)=\boldsymbol{P}+\mathrm{j}\boldsymbol{Q}\\&\qquad \boldsymbol{V}_{\mathrm{lb}}^{\odot2}\leq\mathrm{diag}\left(\dot{\boldsymbol{W}}\right)\leq\boldsymbol{V}_{\mathrm{ub}}^{\odot2}\\&\qquad \boldsymbol{Q}_{\mathrm{lb}}\leq\boldsymbol{Q}\leq\boldsymbol{Q}_{\mathrm{ub}}\end{aligned}\right. \tag{11}$$

where ω_{q} and ω_{v} are the proportional coefficients that satisfy $\omega_{\mathrm{q}}+\omega_{\mathrm{v}}=1$, and their values should be selected to balance the scales of the var margin and voltage deviation objectives, respectively; $\boldsymbol{K}_{\mathrm{q}}$ and $\boldsymbol{K}_{\mathrm{v}}$ are the parameter matrices; $\boldsymbol{Q}_{\mathrm{tar}}$ and $\boldsymbol{V}_{\mathrm{tar}}$ are the target vectors for var and bus voltages, respectively, $\boldsymbol{Q}_{\mathrm{tar}}$ is set to be zero to preserve the var margin in this paper, and $\boldsymbol{V}_{\mathrm{tar}}$ is determined based on the average voltage levels of each bus; $\dot{\boldsymbol{W}}\succcurlyeq0$ denotes that matrix $\dot{\boldsymbol{W}}$ is positive semidefinite; $\boldsymbol{P}+\mathrm{j}\boldsymbol{Q}$ is the complex power injected at the bus; and $\boldsymbol{Q}_{\mathrm{lb}}$ and $\boldsymbol{Q}_{\mathrm{ub}}\in\mathbb{R}^{|\mathcal{N}|}$ are the lower and upper limits of the inductive var injection of $|\mathcal{N}|$ buses, respectively. The Mahalanobis norm of vector $\boldsymbol{x}$ is defined as $\|\dot{\boldsymbol{x}}\|_{\boldsymbol{K}}^2=\dot{\boldsymbol{x}}^{\mathrm{H}}\boldsymbol{K}\dot{\boldsymbol{x}}$, and $\boldsymbol{K}$ is also a parameter matrix. The operation voltage of WT is typically maintained within the range [0.9, 1.1] p.u. to avoid triggering protection systems [21], [22].

B. Volt-var Sensitivity-based Mahalanobis Norm Hyperparameter Setting Method

In the context of wind farm operation, the objective function should be designed to enable the orderly substitution of the var reserve of STATCOM, while ensuring the stable and reliable control of bus voltage. However, previous studies have not specifically addressed the selection of the parameter matrix $\boldsymbol{K}$ for the Mahalanobis norm. Improper selection of $\boldsymbol{K}$ introduces not only numerical instabilities but also operation inefficiencies due to inadequate var output from WTs, ultimately leading to a waste of var resources. This subsection will explore the setting for $\boldsymbol{K}_{\mathrm{q}}$ and $\boldsymbol{K}_{\mathrm{v}}$ to address these concerns.

Since the influence of var compensation on bus voltage diminishes with the increase of electrical distance, voltage regulation at the PCC should prioritize turbines based on the sensitivity of their var output to voltage changes. The Jacobian matrix method is widely used for calculating the volt/var sensitivity matrix [23]. The power flow equations, expressed in polar coordinates in (2), are iteratively solved by:

$$\begin{bmatrix}\Delta \boldsymbol{P}\\ \Delta \boldsymbol{Q}\end{bmatrix}=\begin{bmatrix}\dfrac{\partial \boldsymbol{P}}{\partial|\boldsymbol{V}|} & \dfrac{\partial \boldsymbol{P}}{\partial \boldsymbol{\theta}}\\ \dfrac{\partial \boldsymbol{Q}}{\partial|\boldsymbol{V}|} & \dfrac{\partial \boldsymbol{Q}}{\partial \boldsymbol{\theta}}\end{bmatrix}\begin{bmatrix}\Delta \boldsymbol{V}\\ \Delta \boldsymbol{\theta}\end{bmatrix}=\boldsymbol{J}\begin{bmatrix}\Delta \boldsymbol{V}\\ \Delta \boldsymbol{\theta}\end{bmatrix} \tag{12}$$

where $\boldsymbol{V}$ and $\boldsymbol{\theta}$ are the magnitude and phase angle vectors of the bus voltage, respectively; and Δ denotes the incremental variable. By extracting the relevant elements from the Jacobian matrix, the corresponding volt/var sensitivity for each bus can be determined. When the goal is to bring the var output of STATCOM and WTs to zero, the matrix $\boldsymbol{K}_{\mathrm{q}}\in\mathbb{R}^{|\mathcal{N}|\times|\mathcal{N}|}$ should satisfy the following condition:

$$\boldsymbol{K}_{\mathrm{q}}=\operatorname{diag}\begin{bmatrix}\dfrac{\partial Q_1}{\partial V_{N+2}} & \dfrac{\partial Q_2}{\partial V_{N+2}} & \cdots & \dfrac{\partial Q_N}{\partial V_{N+2}} & 0 & 0 & \varrho & 0\end{bmatrix}^{\mathrm{T}} \tag{13}$$

where $\varrho\in\mathbb{R}^{+}$ is a large enough number. The first N elements of $\boldsymbol{K}_{\mathrm{q}}$ are normalized. The matrix $\boldsymbol{K}_{\mathrm{v}}\in\mathbb{R}^{|\mathcal{N}|\times|\mathcal{N}|}$ should satisfy:

$$\boldsymbol{K}_{\mathrm{v}}=\operatorname{diag}\begin{bmatrix}\underbrace{1\ \ 1\ \ \ldots\ \ 1}_{N} & 0 & 0 & \varrho & 0\end{bmatrix}^{\mathrm{T}} \tag{14}$$

C. Bilinear-OPF Model and Augmented Lagrange Function Formulation

In radial networks, second-order cone relaxation techniques are often employed to accurately convexify the primal problem, enabling easier solutions. Most studies refer to the power flow constraints in (11) as the bus injection model (BIM). In the given network, the primary task of second-order cone relaxation based on the BIM is to transform the semidefinite constraint and rank constraint as:

$$\begin{cases}\dot{\boldsymbol{W}}\succcurlyeq 0\\ rank\left(\dot{\boldsymbol{W}}\right)=1\end{cases}\overset{\dot{\boldsymbol{W}}_{\mathrm{G}}=\dot{\boldsymbol{W}}\odot\boldsymbol{G}}{\Longrightarrow}\begin{cases}\left[\dot{\boldsymbol{W}}_{\mathrm{G}}\right]_{jj}>0\\ \left[\dot{\boldsymbol{W}}_{\mathrm{G}}\right]_{kk}>0\\ \left[\dot{\boldsymbol{W}}_{\mathrm{G}}\right]_{jj}\left[\dot{\boldsymbol{W}}_{\mathrm{G}}\right]_{kk}\geq\left|\left[\dot{\boldsymbol{W}}_{\mathrm{G}}\right]_{jk}\right|^2\\ j,k\in\mathcal{N}\end{cases} \tag{15}$$

where the 0-1 matrix $\boldsymbol{G}$ is the identity matrix plus the adjacency matrix of undirected graph G; $\dot{\boldsymbol{W}}_{\mathrm{G}}$ is the G-partial matrix [14]; and $\left[\dot{\boldsymbol{W}}_{\mathrm{G}}\right]_{jk}$ is the j^{th} row and the k^{th} column element of $\dot{\boldsymbol{W}}_{\mathrm{G}}$.

However, in high-capacitance networks such as offshore wind farms, the amplification of self-admittance weakens the dominance of the largest eigenvalue of the solution $\dot{\boldsymbol{W}}^{*}$ (including $\dot{\boldsymbol{W}}_{\mathrm{G}}^{*}$), leading to voltage distortion and model failure.

A tighter model incorporating cycle conditions or employing semidefinite or chordal relaxation can reduce the distortion, yet reintroduces nonlinearity or nonconvexity, which offsets the benefits of the transformation.

Revisiting the rank constraint optimization in the primal problem, although the ADMM algorithm based on singular value decomposition (SVD) has been validated in applications, the computational efficiency of SVD and the convergence of ADMM algorithm for nonconvex problems remain challenging [24].

Therefore, based on matrix decomposition theory, this paper introduces bilinear matrix equality constraints to replace the rank constraints, which is formulated as:

$$\begin{cases}\dot{\boldsymbol{W}}\succcurlyeq 0\\ rank\left(\dot{\boldsymbol{W}}\right)=1\end{cases}\overset{\dot{\boldsymbol{V}}\approx\dot{\boldsymbol{H}}\approx\dot{\boldsymbol{F}}}{\Longrightarrow}\begin{cases}\dot{\boldsymbol{H}}\rightarrow\dot{\boldsymbol{F}}\\ \dot{\boldsymbol{W}}\rightarrow\dot{\boldsymbol{M}}\\ \dot{\boldsymbol{M}}=\dot{\boldsymbol{H}}\dot{\boldsymbol{F}}^{\mathrm{H}}\end{cases} \tag{16}$$

where $\dot{\boldsymbol{H}},\dot{\boldsymbol{F}}\in\mathbb{C}^{|\mathcal{N}|}$ are the vectors of the bilinear variables, which are introduced to approximate the bus voltages; and $\dot{\boldsymbol{M}}\in\mathbb{C}^{|\mathcal{N}|\times|\mathcal{N}|}$ is used to fit $\dot{\boldsymbol{W}}$. Therefore, the Bilinear-OPF model is reformulated from the primal problem as:

$$\begin{cases}\min\Big(\omega_{\mathrm{q}}\left\|\boldsymbol{Q}-\boldsymbol{Q}_{\mathrm{tar}}\right\|_{\boldsymbol{K}_{\mathrm{q}}}^{2}+\omega_{\mathrm{v}}\left\|\operatorname{diag}\left(\dot{\boldsymbol{W}}\right)-\boldsymbol{V}_{\mathrm{tar}}^{\odot 2}\right\|_{\boldsymbol{K}_{\mathrm{v}}}^{2}+\\ \qquad\gamma_1\left\|\dot{\boldsymbol{H}}-\dot{\boldsymbol{F}}\right\|_{2}^{2}+\gamma_2\left\|\dot{\boldsymbol{M}}-\dot{\boldsymbol{W}}\right\|_{\mathrm{F}}^{2}\Big)\\ \text{s.t. }\ \dot{\boldsymbol{M}}=\dot{\boldsymbol{H}}\dot{\boldsymbol{F}}^{\mathrm{H}}\\ \qquad\mathcal{Y}\left(\dot{\boldsymbol{W}}\right)=\boldsymbol{P}+\mathrm{j}\boldsymbol{Q}\\ \qquad\boldsymbol{V}_{\mathrm{lb}}^{\odot 2}\leq\operatorname{diag}\left(\operatorname{Re}\left(\dot{\boldsymbol{W}}\right)\right)\leq\boldsymbol{V}_{\mathrm{ub}}^{\odot 2}\\ \qquad\boldsymbol{Q}_{\mathrm{lb}}\leq\boldsymbol{Q}\leq\boldsymbol{Q}_{\mathrm{ub}}\end{cases} \tag{17}$$

where γ_1 and γ_2 are the positive coefficients; $\|\cdot\|_2$ denotes the L2-norm; and $\|\cdot\|_{\mathrm{F}}$ denotes the Frobenius norm; and $\operatorname{Re}(\cdot)$ is a function that extracts the real part of variables. To ensure real-valued inequality operations, $\operatorname{diag}\left(\operatorname{Re}\left(\dot{\boldsymbol{W}}\right)\right)$ is used in place of the squared bus voltage magnitude, where the real part transformation on complex variables is $\operatorname{Re}\left(\dot{\boldsymbol{A}}\right)=\left(\dot{\boldsymbol{A}}+\dot{\boldsymbol{A}}^{*}\right)/2$.

This method, which approximates the original rank-constraint optimization problem, eliminates the need for SVD computations and preserves the strong correlation between voltage vectors and matrices.

Additionally, the introduced bilinear constraints and approximation formulas enable each subproblem in the ADMM algorithm to obtain a closed-form solution via the KKT conditions, which significantly improves the computational efficiency [25]. Next, we will discuss the derivation of the augmented Lagrangian function for the problem (17) in the complex domain and the deployment of the ADMM algorithm.

By using Lemma 1 and Lemma 2 from Wirtinger calculus [26] presented in Supplementary Material A, (17) can be reformulated as $\min\mathcal{L}_{\rho}\left(\dot{\boldsymbol{W}},\boldsymbol{Q},\dot{\boldsymbol{M}},\dot{\boldsymbol{H}},\dot{\boldsymbol{F}},\boldsymbol{\eta};\dot{\boldsymbol{\mu}},\dot{\boldsymbol{\Lambda}},\boldsymbol{\lambda}\right)$ given in (18).

$$
\begin{aligned}
\mathcal{L}_{\rho}= & \omega_{\mathrm{q}}\left\|\boldsymbol{Q}-\boldsymbol{Q}_{\mathrm{tar}}\right\|_{\boldsymbol{K}_{\mathrm{q}}}^{2}+\omega_{\mathrm{v}}\left\|\operatorname{diag}\left(\dot{\boldsymbol{W}}\right)-\boldsymbol{V}_{\mathrm{tar}}^{\odot 2}\right\|_{\boldsymbol{K}_{\mathrm{v}}}^{2}+\gamma_{1}\left\|\dot{\boldsymbol{H}}-\dot{\boldsymbol{F}}\right\|_{2}^{2}+ \\
& \gamma_{2}\left\|\dot{\boldsymbol{M}}-\dot{\boldsymbol{W}}\right\|_{\mathrm{F}}^{2}+\rho_{1}\left\|\mathcal{Y}\left(\dot{\boldsymbol{W}}\right)-\boldsymbol{P}-\mathrm{j}\boldsymbol{Q}+\frac{\dot{\boldsymbol{\mu}}}{\rho_{1}}\right\|_{2}^{2}+ \\
& \rho_{2}\left\|\dot{\boldsymbol{M}}-\dot{\boldsymbol{H}}\dot{\boldsymbol{F}}^{\mathrm{H}}+\frac{\dot{\boldsymbol{\Lambda}}}{\rho_{2}}\right\|_{\mathrm{F}}^{2}+\rho_{2}\left\|\dot{\boldsymbol{M}}-\dot{\boldsymbol{H}}\dot{\boldsymbol{F}}^{\mathrm{H}}+\frac{\dot{\boldsymbol{\Lambda}}}{\rho_{2}}\right\|_{\mathrm{F}}^{2}+ \\
& \rho_{\mathrm{qub}}\left\|\boldsymbol{Q}-\boldsymbol{Q}_{\mathrm{ub}}+\boldsymbol{\eta}_{\mathrm{qub}}^{\odot 2}+\frac{\boldsymbol{\lambda}_{\mathrm{qub}}}{\rho_{\mathrm{qub}}}\right\|_{2}^{2}+\rho_{\mathrm{qlb}}\left\|-\boldsymbol{Q}+\boldsymbol{Q}_{\mathrm{lb}}+\boldsymbol{\eta}_{\mathrm{qlb}}^{\odot 2}+\frac{\boldsymbol{\lambda}_{\mathrm{qlb}}}{\rho_{\mathrm{qlb}}}\right\|_{2}^{2}+ \\
& \rho_{\mathrm{vub}}\left\|\frac{1}{2}\operatorname{diag}\left(\boldsymbol{W}+\boldsymbol{W}^{*}\right)-\boldsymbol{V}_{\mathrm{ub}}^{\odot 2}+\boldsymbol{\eta}_{\mathrm{vub}}^{\odot 2}+\frac{\boldsymbol{\lambda}_{\mathrm{vub}}}{\rho_{\mathrm{vub}}}\right\|_{2}^{2}+ \\
& \rho_{\mathrm{vlb}}\left\|-\frac{1}{2}\operatorname{diag}\left(\boldsymbol{W}+\boldsymbol{W}^{*}\right)+\boldsymbol{V}_{\mathrm{lb}}^{\odot 2}+\boldsymbol{\eta}_{\mathrm{vlb}}^{\odot 2}+\frac{\boldsymbol{\lambda}_{\mathrm{vlb}}}{\rho_{\mathrm{vlb}}}\right\|_{2}^{2}
\end{aligned}
\tag{18}
$$

where $\dot{\boldsymbol{\Lambda}} \in \mathbb{C}^{|\mathcal{N}| \times |\mathcal{N}|}$, $\dot{\boldsymbol{\mu}} \in \mathbb{C}^{|\mathcal{N}|}$, and $\boldsymbol{\lambda}_{\mathrm{qub}}, \boldsymbol{\lambda}_{\mathrm{qlb}}, \boldsymbol{\lambda}_{\mathrm{vub}}, \boldsymbol{\lambda}_{\mathrm{vlb}} \in \mathbb{R}^{|\mathcal{N}|}$ are the dual variables; $\eta_{\mathrm{C}} \in \mathbb{R}$ and $\boldsymbol{\eta}_{\mathrm{qub}}, \boldsymbol{\eta}_{\mathrm{qlb}}, \boldsymbol{\eta}_{\mathrm{vub}}, \boldsymbol{\eta}_{\mathrm{vlb}} \in \mathbb{R}^{|\mathcal{N}|}$ are slack variables for the inequality constraints; and ρ_1, ρ_2, ρ_{qub}, ρ_{qlb}, ρ_{vub}, $\rho_{\mathrm{vlb}} \in \mathbb{R}^{+}$ are the update step sizes for the dual variables, which are large enough.

D. Customized ADMM Algorithm

Given the decomposable characteristics of the optimization tasks in the ADMM algorithm, this algorithm has been widely adopted for distributed optimization in power systems [27], [28]. Considering the presence of two convex subproblems in $\mathcal{L}_{\rho}$, namely $\underset{\boldsymbol{W},\boldsymbol{Q},\boldsymbol{F},\boldsymbol{\eta}}{\arg\min}\,\mathcal{L}_{\rho}$ and $\underset{\boldsymbol{M},\boldsymbol{H}}{\arg\min}\,\mathcal{L}_{\rho}$, this paper applies the ADMM algorithm to solve (18). The update strategy for step $k+1$ can be expressed as:

$$
\left(\dot{\boldsymbol{W}},\boldsymbol{Q},\dot{\boldsymbol{F}},\boldsymbol{\eta}\right)^{k+1}=\underset{\dot{\boldsymbol{W}},\boldsymbol{Q},\dot{\boldsymbol{F}},\boldsymbol{\eta}}{\arg\min}\,\mathcal{L}_{\rho}
\tag{19}
$$

$$
\left(\dot{\boldsymbol{M}},\dot{\boldsymbol{H}}\right)^{k+1}=\underset{\dot{\boldsymbol{M}},\dot{\boldsymbol{H}}}{\arg\min}\,\mathcal{L}_{\rho}
\tag{20}
$$

$$
\left(\dot{\boldsymbol{\mu}},\dot{\boldsymbol{\Lambda}},\boldsymbol{\lambda}\right)^{k+1}=\boldsymbol{U}\left(\left(\dot{\boldsymbol{\mu}},\dot{\boldsymbol{\Lambda}},\boldsymbol{\lambda}\right)^{k};\rho\right)
\tag{21}
$$

where $\boldsymbol{U}(\cdot)$ is a set of dual variable update functions dependent on ρ, which will be discussed later. Subproblems (19) and (20) correspond to unconstrained convex quadratic programming and linear programming problems, respectively, and are solved by applying the first-order optimality conditions, specifically the KKT conditions. Based on Wirtinger's conclusions, a variable and its conjugate should be treated as two independent variables when applying the KKT conditions. The first-order optimality conditions are presented in Supplementary Material A. Consequently, the ADMM algorithm, deployed at the AVC substation to solve the Bilinear-OPF model in a centralized manner, is derived. The details are provided in Algorithm 1, where variables with superscript "▲" refers to the final results.

IV. Asynchronous Hierarchical Control Scheme

Centralized method has been successfully implemented based on the previous derivation of the Bilinear-OPF model and the ADMM algorithm. This section further explores the design of an asynchronous hierarchical control scheme.

Algorithm 1: customized ADMM algorithm for $\mathcal{L}_{\rho}$ processed by AVC substation

Input: problem parameters $\boldsymbol{K}_{\mathrm{q}}, \boldsymbol{P}, \boldsymbol{Q}_{\mathrm{tar}}, \dot{\boldsymbol{Y}}_{\mathrm{GB}}, \dot{\boldsymbol{X}}_{l}, \boldsymbol{A}, \rho, \boldsymbol{Q}_{\mathrm{ub}}, \boldsymbol{Q}_{\mathrm{lb}}, \boldsymbol{V}_{\mathrm{ub}}, \boldsymbol{V}_{\mathrm{lb}}$ and initial point $\left(\dot{\boldsymbol{W}}^{0}, \boldsymbol{Q}^{0}, \dot{\boldsymbol{M}}^{0}, \dot{\boldsymbol{H}}^{0}, \dot{\boldsymbol{F}}^{0}, \dot{\boldsymbol{\mu}}^{0}, \dot{\boldsymbol{\Lambda}}^{0}, \boldsymbol{\lambda}^{0}, \boldsymbol{\eta}^{0}\right)$

Output: local minimizer $\left(\dot{\boldsymbol{W}}, \boldsymbol{Q}, \dot{\boldsymbol{M}}, \dot{\boldsymbol{H}}, \dot{\boldsymbol{F}}\right)$

1. **while** $\mathcal{L}_{\rho}$ has not converged **do**
2. Update $\dot{\boldsymbol{W}}$, $\boldsymbol{Q}$, $\dot{\boldsymbol{F}}$, and $\boldsymbol{\eta}$
   Obtain $\left(\dot{\boldsymbol{W}}, \boldsymbol{Q}, \dot{\boldsymbol{F}}, \boldsymbol{\eta}\right)^{k+1}$ by solving (SA3), (SA4), (SA6), and (SA10) in Supplementary Material A
3. Update $\dot{\boldsymbol{M}}$ and $\dot{\boldsymbol{H}}$
   Obtain $\left(\dot{\boldsymbol{M}}, \dot{\boldsymbol{H}}\right)^{k+1}$ by solving (SA5) and (SA7) in Supplementary Material A
4. Update $\dot{\boldsymbol{\mu}}$, $\dot{\boldsymbol{\Lambda}}$, and $\boldsymbol{\lambda}$
   Obtain $\left(\dot{\boldsymbol{\mu}}, \dot{\boldsymbol{\Lambda}}, \boldsymbol{\lambda}\right)^{k+1}$ by solving (SA11) in Supplementary Material A
5. $k=k+1$
6. **end while**
7. Return $\dot{\boldsymbol{W}}^{▲}$, $\boldsymbol{Q}^{▲}$, $\dot{\boldsymbol{M}}^{▲}$, $\dot{\boldsymbol{H}}^{▲}$, and $\dot{\boldsymbol{F}}^{▲}$

From the control perspective, this section introduces a grouping strategy for WTs based on network topology to address the compatibility issues posed by point-to-point communication on outdated communication devices. A master-slave multi-agent system is employed to coordinate inter-group and intra-group communication and control within the hierarchical structure.

From the algorithmic perspective, following the turbine grouping rules, the proximal Jacobian ADMM algorithm is leveraged to extend Algorithm 1 into a block-wise parallel computing framework (i.e., parallel ADMM algorithm). Extensive numerical experiments have demonstrated that multi-block ADMM algorithm exhibits strong asynchronous convergence properties, providing theoretical support for hierarchical control [29], [30].

A. Illustration of Asynchronous Hierarchical Control Scheme

In the offshore wind farm illustrated in Fig. 1, 4-6 WTs are typically connected in parallel to form a subgroup, sharing a single collector line for power transmission. Utilizing this characteristic, this paper divides the wind farm into a multi-agent system. It consists of a master-agent region formed by the substation and switching station, and slave-agent regions formed by each subgroup.

The master agent is installed at the AVC substation. Its responsibilities include receiving the status of subgroups from the slave agents, and sharing the information of STATCOM, on-load tap-changing transformer status, and global power flow with the slave agents. Slave agents are located at the WT controller nearest to the OLTC in each subgroup. Their tasks include calculating the var commands for all WTs within the subgroup, transmitting the local operation status to the master agent, and issuing the control commands to other WTs in the subgroup. An illustration of this master-slave agent system is shown in Fig. 2, where C is the number of agent regions; and n is the set of subgroups, $n=\{n_1, n_2, ..., n_C\}$.

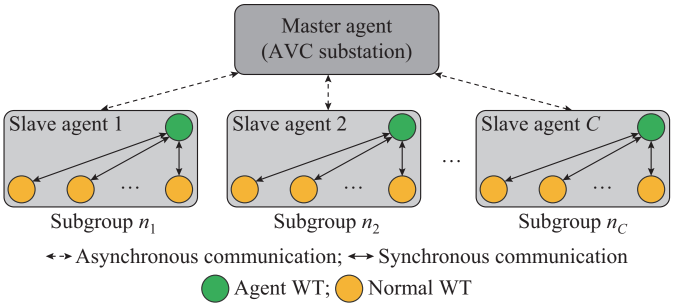

Fig. 2. Illustration of master-slave agent system.

As for computational burden, agents must solve optimization problems to generate control commands. However, the efficiency of the ADMM algorithm is highly sensitive to changes at the initial point, making it challenging to predict the time required for the agents [31]. Therefore, asynchronous communication is implemented. Since the communication between WTs and slave agents only involves uploading and downloading the operation status and control commands, synchronous communication is used to ensure the control effectiveness.

Given the differences in the redundancy of communication devices across the aging offshore wind farms, the communication method is based on the data exchange capacity of the original control systems to preserve generality. The internal node communication method, originally used in the centralized control of aging offshore wind farms, is applied to the communication between master and slave agents for enhanced compatibility, which also supports the listening of ports and on-demand communication. Moreover, memory-sharing eliminates the redundancy caused by multiple data copies, and delivers high communication efficiency in networks with limited processors, making it well-suited for synchronous communication between slave agents and WTs.

Figure 3 illustrates the working timeline of the asynchronous hierarchical control scheme for online coordination. It prevents the loss of solution timeliness by waiting for all agent tasks to be completed. Also, if communication fails, the remaining subgroups can still complete the global optimization with limited degrees of freedom, providing resilience to interference. The "Troubleshooting" section in Fig. 3 summarizes the response of the asynchronous hierarchical control scheme to the operation of common agents under abnormal conditions. The purple dashed curve in Fig. 3 denotes the duration of a failure spanning a certain length. The orange dashed line denotes the uncertain delay in data transmission caused by the failure, with the delay duration determined by the failure duration. Four cases are described as follows.

1) Case 1

In Case 1, the computation does not converge. Although existing studies suggest that the parallel ADMM algorithm guarantees convergence under static conditions, the randomness of WT output may introduce specific challenges. To ensure redundancy, if non-convergence occurs, the slave agent will retain the previous value in the next cycle and upload it to the master agent, while the turbine cluster will not receive var instructions during this period.

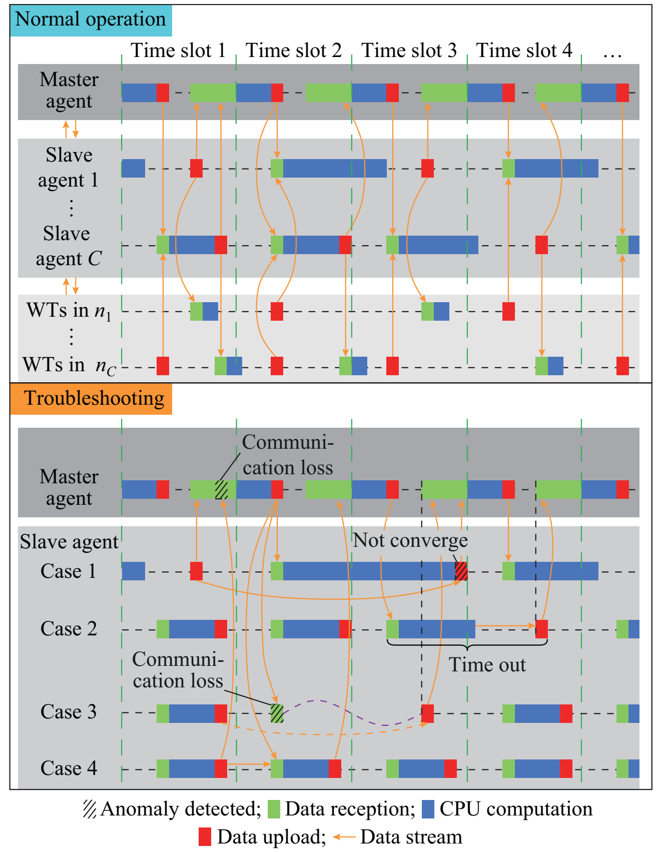

Fig. 3. Working timeline of asynchronous hierarchical control scheme.

2) Case 2

In Case 2, the computation converges but exceeds the time limit, and the slave agent will wait until the next cycle to upload the optimized solution. Meanwhile, the turbine cluster will use the previously optimized solution as its var command.

3) Case 3

In Case 3, the communication from master agent to slave agent fails. The slave agent does not compute subtasks, and the WTs in this subgroup does not receive var instructions. Once communication is restored, the slave agent will upload the last optimized solution to the master agent as the output.

4) Case 4

In Case 4, the communication from slave agent to master agent fails. The slave agent receives signals from the master agent in the next cycle and proceeds with subtask calculations as usual. Notably, the master agent does not update global information for the fault agent during this period.

During failures, in Cases 1-3, the subgroups without fault and STATCOMs will provide var and voltage control redundancy. While in Case 4, redundancy is provided by the fault subgroup and STATCOM.

Considering the worst case, it is assumed that the wind farm uses broadband carrier communication from WT to substation. The orthogonal frequency division multiplexing technology [32] is used between nodes with robust modulation employed.

If the throughput for a single communication between a WT and the substation is approximately D_{WT} bits, the total throughput for collecting data from all N WTs will be ND_{WT}

bits. The channel capacity C_{WT} is determined by Shannon's law. Hence, for traditional control methods, the minimum theoretical time for the data collection at AVC substation is approximately $ND_{\mathrm{WT}}/C_{\mathrm{WT}}$ for each time.

In the asynchronous hierarchical control scheme, the number of slave agents is assumed to be $N/5$, with the throughput for a single communication being approximately $5\upsilon D_{\mathrm{WT}}$ bits, where υ is the communication throughput reduction factor due to data packaging for all WTs in the subgroup ($0<\upsilon<1$). υ decreases as more WTs participate in the subgroup. Thus, in the proposed AHVC method, the minimum time for the master agent to collect data from all slave agents in each cycle is $\upsilon ND_{\mathrm{WT}}/C_{\mathrm{WT}}$. Additionally, considering the average idle time Δt between consecutive communications, the proposed AHVC method saves $(1-\upsilon)ND_{\mathrm{WT}}/C_{\mathrm{WT}}+0.8N\Delta t$ of communication time. As a result, it significantly reduces the channel occupancy of the AVC substation.

B. Formulation of Subproblem for Slave Agent Based on Parallel ADMM Algorithm

Next, this paper will discuss the specific optimization task for the slave agent. Assume that the wind farm is divided into $|n|=C$ agent regions, and the subsets satisfy $\sum_i |n_i| = N+3$. Taking the agent in region n_i as the focus, the $|n|$-block problem is decomposed from (18) and expressed as:

$$\begin{aligned}\mathcal{L}_{J,\rho} = {} & \omega_{\mathrm{q}} \sum_{i=1}^{|n|} \left\| \boldsymbol{Q}_{n_i} - \boldsymbol{Q}_{\mathrm{tar},n_i} \right\|_{\boldsymbol{K}_{\mathrm{q}}}^2 + \omega_{\mathrm{v}} \left\| \mathrm{diag}\left(\dot{\boldsymbol{W}}\right) - \boldsymbol{V}_{\mathrm{tar}}^{\odot 2} \right\|_{\boldsymbol{K}_{\mathrm{v}}}^2 + \\ & \gamma_1 \left\| \dot{\boldsymbol{H}} - \dot{\boldsymbol{F}} \right\|_2^2 + \gamma_2 \left\| \dot{\boldsymbol{M}} - \dot{\boldsymbol{W}} \right\|_{\mathrm{F}}^2 + \\ & \rho_1 \left\| \mathcal{Y}\left(\dot{\boldsymbol{W}}\right) - \left(\boldsymbol{P} + \mathrm{j}\boldsymbol{Q}\right) + \frac{\dot{\boldsymbol{\mu}}}{\rho_1} \right\|_2^2 + \\ & \rho_2 \left\| \dot{\boldsymbol{M}} - \frac{\dot{\boldsymbol{H}}\dot{\boldsymbol{F}}^{\mathrm{H}} + \dot{\boldsymbol{F}}\dot{\boldsymbol{H}}^{\mathrm{H}}}{2} + \frac{\dot{\boldsymbol{\Lambda}}}{\rho_2} \right\|_{\mathrm{F}}^2 + \\ & \rho_{\mathrm{qub}} \sum_{i=1}^{|n|} \left\| \boldsymbol{Q}_{n_i} - \boldsymbol{Q}_{\mathrm{ub},n_i} + \boldsymbol{\eta}_{\mathrm{qub},n_i}^{\odot 2} + \frac{\boldsymbol{\lambda}_{\mathrm{qub},n_i}}{\rho_{\mathrm{qub}}} \right\|_2^2 + \\ & \rho_{\mathrm{qlb}} \sum_{i=1}^{|n|} \left\| -\boldsymbol{Q}_{n_i} + \boldsymbol{Q}_{\mathrm{lb},n_i} + \boldsymbol{\eta}_{\mathrm{qlb},n_i}^{\odot 2} + \frac{\boldsymbol{\lambda}_{\mathrm{qlb},n_i}}{\rho_{\mathrm{qlb}}} \right\|_2^2 + \\ & \rho_{\mathrm{vub}} \left\| \frac{\mathrm{diag}\left(\boldsymbol{W}+\boldsymbol{W}^*\right)}{2} - \boldsymbol{V}_{\mathrm{ub}}^{\odot 2} + \boldsymbol{\eta}_{\mathrm{vub}}^{\odot 2} + \frac{\boldsymbol{\lambda}_{\mathrm{vub}}}{\rho_{\mathrm{vub}}} \right\|_2^2 + \\ & \rho_{\mathrm{vlb}} \left\| -\frac{\mathrm{diag}\left(\boldsymbol{W}+\boldsymbol{W}^*\right)}{2} + \boldsymbol{V}_{\mathrm{lb}}^{\odot 2} + \boldsymbol{\eta}_{\mathrm{vlb}}^{\odot 2} + \frac{\boldsymbol{\lambda}_{\mathrm{vlb}}}{\rho_{\mathrm{vlb}}} \right\|_2^2 \end{aligned} \tag{22}$$

where the subscript n_i of a matrix indicates that only the row and column corresponding to the bus numbers in n_i are retained, while all other elements are set to be 0. Similarly, the subscript n_i of a vector indicates that only the elements corresponding to the bus numbers in set n_i are retained, with all other elements set to be 0. Compared with (18), (22) adopts the following symmetric form to ensure the synchronous update of the bilinear variables $\dot{\boldsymbol{H}}$ and $\dot{\boldsymbol{F}}$ in $\mathcal{L}_{J,\rho}$:

$$\dot{\boldsymbol{H}}\dot{\boldsymbol{F}}^{\mathrm{H}} \approx \dot{\boldsymbol{F}}\dot{\boldsymbol{H}}^{\mathrm{H}} \approx \frac{1}{2}\sum_{i=1}^{\mathrm{C}}\left(\dot{\boldsymbol{H}}_{n_i}\dot{\boldsymbol{F}}^{\mathrm{H}} + \dot{\boldsymbol{F}}_{n_i}\dot{\boldsymbol{H}}^{\mathrm{H}}\right) \tag{23}$$

C. Update of |n|-block Variables in Agents Based on Parallel ADMM Algorithm

Similarly, due to the implicit function constraints of the power flow equations, the update of $|n|$-block is only available for variable $\boldsymbol{Q}$ via the KKT conditions, as shown in (SA12) in Supplementary Material A. Moreover, this paper introduces a proximal term $\frac{1}{2}\left\|\boldsymbol{Q}_{n_i} - \boldsymbol{Q}_{n_i}^k\right\|_{\boldsymbol{\tau}}^2$ to avoid ill-conditioned cases, where $\boldsymbol{\tau}$ is a constant matrix that may be either an identity matrix or a matrix of ones. The damping coefficient $\vartheta>0$ is applied to the dual variables.

The details of parallel ADMM algorithm are provided in Algorithm 2.

Algorithm 2: parallel ADMM algorithm for $\mathcal{L}_{J,\rho}$ processed by slave agent

Preset: parameters $\boldsymbol{K}_{\mathrm{q}}, \boldsymbol{Q}_{\mathrm{tar},n_i}, \dot{\boldsymbol{Y}}_{\mathrm{GB}}, \dot{\boldsymbol{X}}_l, \boldsymbol{A}, \rho, \boldsymbol{Q}_{\mathrm{ub},n_i}, \boldsymbol{Q}_{\mathrm{lb},n_i}, \boldsymbol{V}_{\mathrm{ub},n_i}$, and $\boldsymbol{V}_{\mathrm{lb},n_i}$

Global sharing: receive initial point $\left(\dot{\boldsymbol{W}}^0, \boldsymbol{Q}^0, \dot{\boldsymbol{M}}^0, \dot{\boldsymbol{H}}^0, \dot{\boldsymbol{F}}^0\right)$ and parameters $\left(\boldsymbol{P}, \boldsymbol{V}_{\mathrm{ub}}, \boldsymbol{V}_{\mathrm{lb}}\right)$ from AVC substation

Local upload: upload parameters $\left(\boldsymbol{P}_{n_i}, \boldsymbol{Q}_{\mathrm{ub},n_i}, \boldsymbol{Q}_{\mathrm{lb},n_i}\right)$ from WTs in n_i

Reset $\left(\dot{\boldsymbol{\mu}}, \dot{\boldsymbol{\Lambda}}, \boldsymbol{\lambda}\right)$ to unit scalar/vector/matrix, and reset $\boldsymbol{\eta}$ to be zero

Output: local minimizer $\boldsymbol{Q}_{n_i}$

1. **while** $\mathcal{L}_{J,\rho}$ does not converge **do**
2. Update $\dot{\boldsymbol{W}}, \boldsymbol{Q}_{n_i}, \dot{\boldsymbol{F}}$, and $\boldsymbol{\eta}$
   Obtain $\left(\dot{\boldsymbol{W}}, \boldsymbol{Q}_{n_i}, \dot{\boldsymbol{F}}, \boldsymbol{\eta}\right)^{k+1}$ by solving (SA3), (SA6), (SA12), and (SA13) in Supplementary Material A
3. Update $\dot{\boldsymbol{M}}$ and $\dot{\boldsymbol{H}}$
   Obtain $\left(\dot{\boldsymbol{M}}, \dot{\boldsymbol{H}}\right)^{k+1}$ by solving (SA5) and (SA7) in Supplementary Material A
4. Update $\dot{\boldsymbol{\mu}}, \dot{\boldsymbol{\Lambda}}$, and $\boldsymbol{\lambda}$
   Obtain $\left(\dot{\boldsymbol{\mu}}, \dot{\boldsymbol{\Lambda}}, \boldsymbol{\lambda}\right)^{k+1}$ by solving (SA14) in Supplementary Material A
5. $k=k+1$
6. **end while**
7. Return $\boldsymbol{Q}_{n_i}^{\blacktriangle}$

In practice, the STATCOM performs real-time voltage control at the PCC. As a result, the AVC substation is not responsible for handling the optimization tasks in the proposed AHVC method.

D. Online Implementation of WTs

As discussed earlier, the var limit of each WT is closely tied to its active power output status. For full-scale WTs, the feasible region $\mathcal{Q}$ for var is determined by the capacity of the converter:

$$P_{\mathrm{WT}}^2 + Q_{\mathrm{GSC}}^2 \le S_{\mathrm{GSC}}^2 \tag{24}$$

where P_{WT} is the active power output of the WT, which is determined by the air energy captured by the wind rotor; and Q_{GSC} and S_{GSC} are the var output and capacity of the GSC in WT, respectively.

The var output reference value of WT is issued by the slave agent. However, small fluctuations in active power output during the optimization can cause instability in the var limits. To ensure real-time control in practical applications, the var command at time t should be projected into the feasible region to get:

$$Q_j^{\mathrm{ref},\blacktriangle}(t) = proj_{\mathcal{Q}}\left[Q_j^{\blacktriangle}(t)\right] \quad \forall j \in \{1,2,\ldots,N\} \tag{25}$$

where superscript "ref" denotes the control command after the projection operation $proj_{\mathcal{Q}}[\cdot]$ at $\mathcal{Q}$.

V. Case Studies

This section presents the case studies to evaluate the effectiveness and accuracy of the Bilinear-OPF model. The parallel ADMM algorithm is implemented in MATLAB/Simulink environment in a computer with Intel Core i5 @ 3.70 GHz and 32 GB RAM. The convergence tolerance is 10^{-6} p.u.. The 78-node test system used in this paper, as shown in Fig. SA1 in Supplementary Material A, is based on data from an offshore wind farm in southern China. The simulation includes two cases: a static case and a dynamic case. The static case is designed to examine the optimization performance and convergence of the proposed algorithm under fixed WT loads. Then, the dynamic case compares the control performance of different control methods when WT loads fluctuate, given the same communication and computational conditions.

The wind farm is composed of 73 WTs, each with a capacity of 5.5 MVA, grouped into 16 subgroups that connect to the low-voltage side of the booster station. After stepping up the voltage from 35 kV to 220 kV, the power is transmitted via submarine cables to the onshore switching station. The switching station is equipped with two ±45 Mvar STATCOMs. To simulate an aging wind farm with a low-capacity STATCOM configuration, one STATCOM is in operation, and the other one is on standby.

A. Static Performance

The heatmap in Fig. SA2 in Supplementary Material A illustrates the volt/var sensitivity matrix of the 78-bus test system. By disregarding sensitivities below 0.03 p.u./p.u., it can be observed that the var output of WTs within a subgroup primarily affects the voltage of that subgroup or the PCC. Moreover, as the electrical distance between a WT and the PCC increases, the influence of the var output of WT on the PCC voltage decreases. Then, the specific values of $\boldsymbol{K}_{\mathrm{q}}$ required in (13) can be found in the PCC bus row of the sensitivity matrix, i.e., row 76.

1) Accuracy of Power Flow Constraints

This part evaluates the accuracy of power flow constraints in offshore wind farm environments across different models, as the inductive var output from all power sources gradually increases from −100% to 100%. By using Simulink results as a reference, comparisons are made between the second-order cone model (DistFlow) with second-order cone programming, decoupled linearized power flow (DLPF) model with linear programming, and the sensitivity estimation model (Sen.) [33]. The exact bilinear model using ADMM is distinguished as "Exact Bilinear" [25].

Figure 4 provides a summary of accumulative error of bus voltage ϵ_{ACC} defined in (26), while Fig. SA3 in Supplementary Material A shows part of the results of static voltage curves.

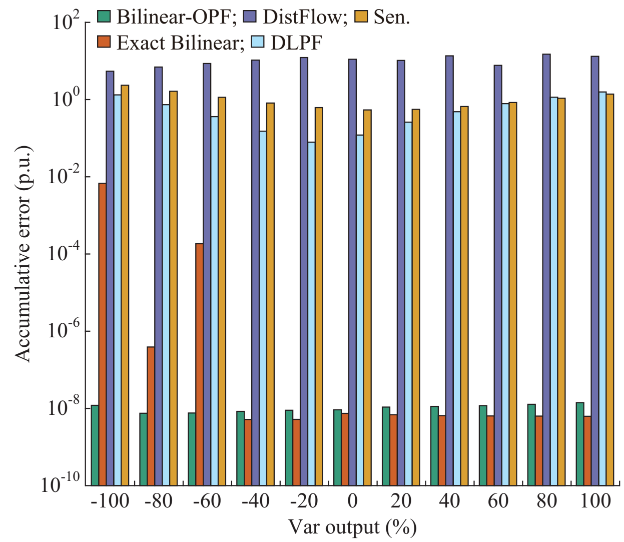

Fig. 4. Accumulative error of bus voltage.

$$\epsilon_{\mathrm{ACC}} = \left\| \boldsymbol{V}_{\mathrm{oprt}} - \boldsymbol{V}_{\mathrm{tar}} \right\|_1 \tag{26}$$

where $\boldsymbol{V}_{\mathrm{oprt}}$ is the vector that records the operation values of bus voltages.

In the statistical results, two bilinear variable-based models exhibit a maximum accumulative error of 2×10^{-8} p.u. across all scenarios, which is significantly lower than those of other models. In contrast, the Exact Bilinear model exacerbates the capacitive characteristics of the grid due to excessive var output, leading to inaccuracies under extreme conditions, such as the var output under range $[-100\%, -55\%]$. Compared with the Bilinear-OPF model, the Exact Bilinear model lacks one degree of freedom in the voltage matrix, making it more challenging to solve and resulting in poorer convergence, with voltage distortions ranging from 2×10^{-7} p.u. to 9×10^{-3} p.u..

Additionally, due to the loose convex relaxation of power flow constraints, the DistFlow and DLPF models exhibit accumulative errors of bus voltage ranging from 0.1 p.u. to 1 p.u.. The Sen. model typically relies on first-order sensitivity, making it suitable only for small-scale var changes near the measurement points, such as around 0%. As a result, with the increase in var output, the error is amplified, ranging from 0.6 p.u. to 5 p.u..

Figure SA3 in Supplementary Material A shows the voltage profile under certain conditions, which is consistent with the conclusions drawn from Fig. 4. In summary, only the Bilinear-OPF model can maintain accuracy and stability when the var output of the WT fluctuates.

2) Optimality of Hyperparameter

This part evaluates the optimization effects of different objective hyperparameters, as shown in Fig. 5. Here, K_{q1} or K_{v1} to K_{q4} or K_{v4} represent the hyperparameters of four cases described as follows: ① $\boldsymbol{K}_{\mathrm{q}}$ or $\boldsymbol{K}_{\mathrm{v}}$ with volt/var sensitivity-based Mahalanobis norm hyperparameter setting method; ② a unit matrix setting method; ③ an empirical diagonal matrix setting method; and ④ a random symmetric matrix setting method. These tests are carried out based on the Bilinear-OPF model.

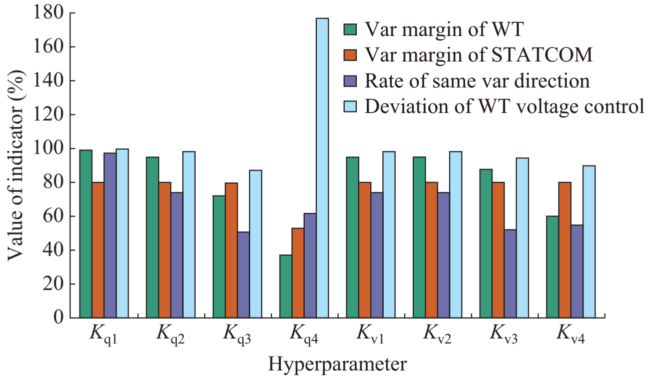

Fig. 5. Optimization effects of different objective hyperparameters.

The comparison between the volt/var sensitivity-based Mahalanobis norm hyperparameter setting method and the unit matrix setting method reveals that the former greatly enhances the coordination performance of var dispatch across WTs. This improvement helps conserve the var margin by avoiding var circulation. Additionally, the optimized setting of $\boldsymbol{K}_q$ and $\boldsymbol{K}_v$ enhances the results over the empirical method, with $\boldsymbol{K}_q$ having a greater impact than $\boldsymbol{K}_v$. Furthermore, using a randomized method disrupts the diagonal matrix format, leading the Bilinear-OPF model to degenerate into a nonlinear form, which can cause difficulties in the solution or entrapment in local optima.

3) Optimality of Models

This part evaluates the optimal solutions and optimization performance of all referenced models using the primal problem as the optimization objective. Figure SA4 in Supplementary Material A presents the var output of the slave-agent WTs, with static optimization results provided in Table I.

TABLE I
COMPARISON OF STATIC OPTIMIZATION RESULTS

Model	Reactive power margin of WTs (Mvar)	Reactive power margin of STATCOM (Mvar)	Accuracy deviation of voltage control (p.u.)	Number of WTs with var margin of less than 10%	Number of WTs with voltage deviation of more than 0.01 p.u.	Accuracy error of bus voltage (p.u.)
Bilinear-OPF	185.64	86.62	0.34	22	0	0.33
Exact Bilinear	5.09	89.91	7.65	70	74	7.55
Dist-Flow	11.61	12.68	7.37	67	74	7.23
DLPF	306.01	37.97	1.12	4	70	0.11
Sen.	56.04	0.00	0.87	56	34	0.55

The optimal solutions of the Bilinear-OPF, Exact Bilinear, and DistFlow models are similar. However, due to cumulative errors exceeding 7.23 p.u. in the latter two models, the var output of non-agent WTs becomes disordered, resulting in an insufficient var margin. For the Bilinear-OPF model, the var output of WTs is about 53.8% of the total wind farm capacity, while for the Exact Bilinear and DistFlow models, it exceeds 97.1%. Furthermore, the accumulative deviation of voltage control for these two models is greater than 1.0 p.u., indicating a failure in control. Although the DLPF model achieves a more considerable var margin, its control performance is poor. The nonlinear volt/var relationship in the 35 kV system causes the approximation errors of the volt/var sensitivity-based Mahalanobis norm hyperparameter setting method to produce var outputs in the wrong direction, requiring complete occupation of STATCOM to compensate for these errors. While voltage control is eventually achieved, the cost is unacceptable.

4) Convergence Performance

Figure 6 shows the convergence performances of different models, where the red dashed line represents the criterion of convergence, i.e., 5×10^{-3}. The ADMM-based models iterate using the KKT conditions, the DistFlow model is solved using a second-order cone programming solver, and both the DLPF and Sen. models use linear solvers.

The collector grid of an offshore wind farm is a medium-to-small-scale network. Due to its topology, the var optimization task is naturally decomposed into subtasks. As a result, adopting a distributed algorithm can achieve significant convergence performance.

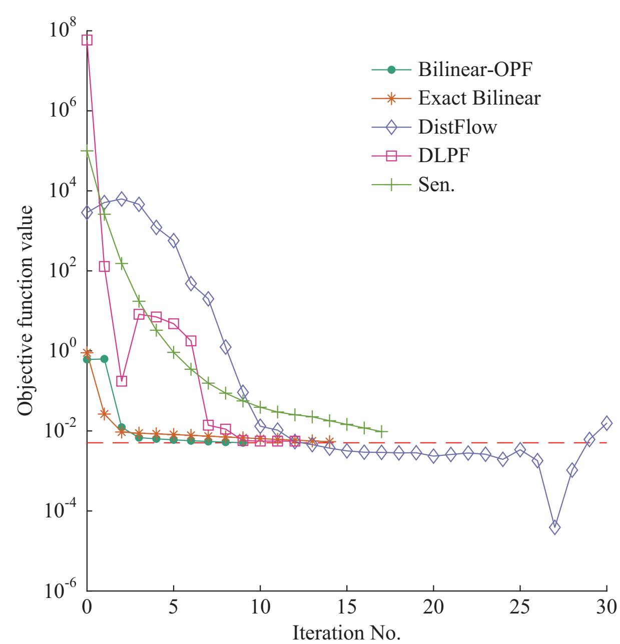

Fig. 6. Convergence performances of different models.

Under the same computational efficiency, the Bilinear-OPF model reduces the computation time by 42.1% compared with Exact Bilinear, 70.5% compared with DistFlow model, 66.7% compared with DLPF model, and 76.5% compared with Sen. model.

B. Dynamic Performance

The dynamic test is conducted in a Simulink environment and lasts for 15 min. The slack bus voltage is held constant at 1.0 p.u., while the active power output of WTs is illustrated in Fig. SA5 in Supplementary Material A.

Based on the transformer tap interval of 1.25%, this paper evaluates the performance of the collector grid under a 0.02 p.u. shift in PCC voltage. The test is conducted in three stages. ① Stage 1 (0-300 s): the AVC substation does not receive any voltage command, and the primary STATCOM is on standby. ② Stage 2 (300-600 s): the PCC voltage setpoint is 1.07-1.08 p.u.. ③ Stage 3 (600-900 s): the PCC voltage setpoint is 1.06-1.07 p.u..

1) Optimality

The voltage profiles of wind farm in Fig. 7 show the range of voltage fluctuations in the collector grid when only STATCOM is used for voltage control, with the voltage levels decreasing from Stage 1 to Stage 3 in the respective curve clusters.

The centralized control method, limited by a communication interval of no less than 5 min, performs offline optimization only at 300 s and 600 s. This causes real-time voltage control to rely solely on STATCOM during the optimization gaps, preventing timely adjustments to WTs with significant active power fluctuations. Additionally, in MPPT mode, when the converter reaches its power limit, it prioritizes reducing the var output, which further widens real-time voltage deviations. The operation range of the converter is typically within ±10% of the nominal voltage. In this case, the centralized control method results in overvoltage condition that lasts for 245 s, clearly underperforming the distributed and hierarchical control methods.

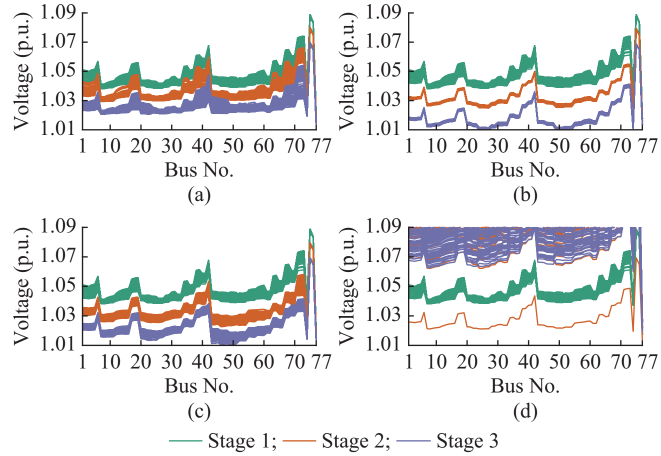

Fig. 7. Voltage profiles of wind farm. (a) Raw. (b) Bilinear-OPF model. (c) DLPF model. (d) DistFlow model.

The datasets with 0% communication failure rate in Fig. SA7 in Supplementary Material A show the var output curve of the STATCOM. Table II summarizes the comparison of dynamic control robustness, including the maximum voltage fluctuation of WT, the working time of the standby STATCOM, and the minimum margin of STATCOM, and the average benefit-cost ratio for each stage. In Table II, the maximum/minimum var margins of STATCOM record the var margins of main and standby STATCOMs with symbol “+”, respectively. Overall, under ideal conditions, the proposed AHVC method provides optimal WT voltage control while eliminating the need for additional STATCOM activation to maintain stability.

TABLE II
COMPARISON OF DYNAMIC CONTROL ROBUSTNESS

Model (control method)	Stage	Communication failure of 0%				Communication failure of 20%				Communication failure of 40%			
		Maximum voltage fluctuation of WT (p.u.)	Working time of standby STATCOM (s)	Minimum var margin of STATCOM (Mvar)	Average benefit-cost ratio (%)	Maximum voltage fluctuation of WT (p.u.)	Working time of standby STATCOM (s)	Minimum var margin of STATCOM (Mvar)	Average benefit-cost ratio (%)	Maximum voltage fluctuation of WT (p.u.)	Working time of standby STATCOM (s)	Minimum var margin of STATCOM (Mvar)	Average benefit-cost ratio (%)
Bilinear-OPF (hierarchical)	2	0.0011	0	17.0+45	92.81	0.0022	0	15.9+45	91.17	0.0024	0	14.2+45	88.62
	3	0.0019	0	21.8+45	100.00	0.0023	0	13.5+45	87.57	0.0027	0	13.8+45	88.02
DLPF (distributed)	2	0.0023	0	8.9+45	83.18	0.0035	0	2.9+45	73.92	0.0093	105	0+28.8	44.44
	3	0.0051	0	19.8+45	100.00	0.0068	0	0.8+45	70.68	0.0110	210	0+19	29.32
DistFlow (centralized)	2	0.0710	300	0	0.00	0.0071	300	0	0	0.0710	300	0	0.00
	3	0.0930	300	0	0.00	0.0093	300	0	0	0.0930	300	0	0.00

2) Computation and Communication Overhead

Figure 8 illustrates the dynamic convergence performance of each model, using the number of iterations as the time unit. To eliminate discrepancies caused by computational performance, it is assumed that each iteration takes the same amount of time. The observed entities for the hierarchical, distributed, and centralized control methods are the slave-agent controller, WT controller, and AVC substation. Owing to the substantial reduction of decentralized control methods in the searching domain of the optimization problem, the computation time per iteration improves by at least 84.4% compared with the centralized control method. Additionally, the limited scope of decision variables reduces the initial offset of Lagrange multiplier based models, including the Bilinear-OPF model. In the Bilinear-OPF model, the objective function value drops to 0.2 after the first optimization. In contrast, in the distributed control method, it remains above 1×10^7, showing that the optimal solution is much closer to the initial value in the former.

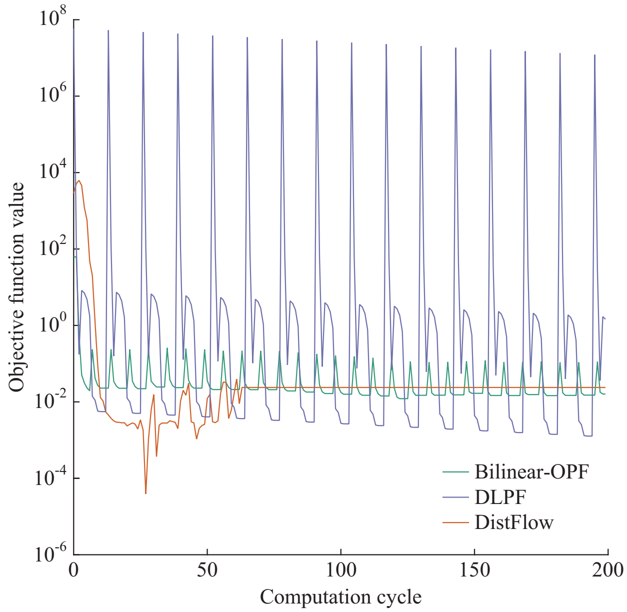

Fig. 8. Dynamic convergence performance.

Without constraints on the communication capacity, the average data throughput across the network is shown in Fig. 9. It is important to note that the DLPF model, using P2P communication, involves large-scale uncoordinated small packet transfers, with download and upload rates consistently exceeding 511 Kb/s. Since the Bilinear-OPF model has slave-agents packaging data from all WTs within a subgroup, it eliminates 78.5% of the handshake packet data compared with the many-to-one upload of the centralized control method. While its single transmission rate is slightly lower than the DistFlow model, it is easier to be implemented on existing hardware platforms.

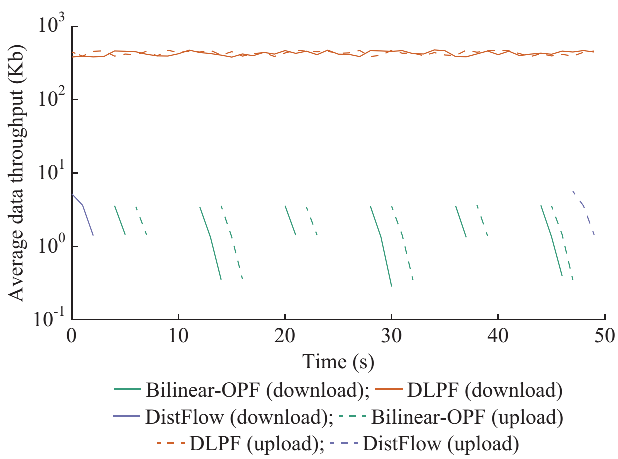

Fig. 9. Average data throughput.

3) Robustness

This part examines the contribution of the proposed AHVC method in mitigating oscillations of the initial value in the ADMM algorithm under normal conditions, and evaluates its control robustness under abnormal conditions based on the "Troubleshooting" section outlined in Fig. 3.

The following assumptions are made to ensure a controlled testing environment. ① The dataset is extracted from a 40 s segment of Fig. SA5 in Supplementary Material A. ② The computation time limit in Algorithm 2 for all agents is set to be 1 s. ③ The active power output of WT updates every 10 s to provide sufficient convergence time for the blockwise ADMM algorithm. ④ The var output of WT updates every 1 s to maintain real-time response.

Firstly, to quantify the influence of AHVC initialization, Fig. 10 compares the var output oscillations of the initial subgroup between the traditional random initialization method with the proposed AHVC method during the $|n|$-block ADMM iterations. The stacked bar chart (left y-axis) represents the var output of subgroups 1-16 (from bottom to top, respectively), with distinct colors corresponding to different subgroups. The iteration residual is represented by the blue curves with circles (right logarithmic y-axis), illustrating the convergence behavior of the var output of subgroups.

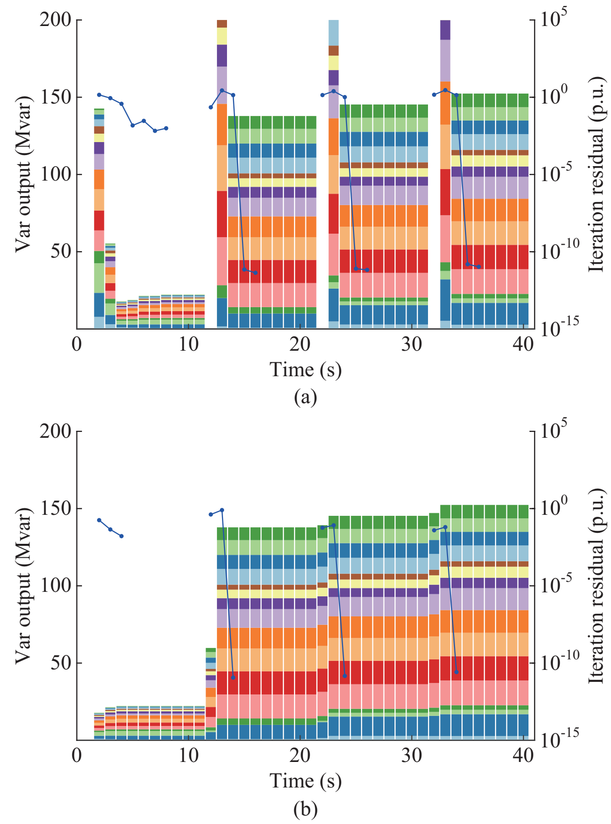

Fig. 10. Comparison of var output oscillations of initial subgroup. (a) Traditional random initialization method. (b) Proposed AHVC method.

Observations indicate that the traditional random initialization method exhibits significant var spikes across multiple subgroups at each active power update interval (every 10 s). Consequently, the initial convergence time for traditional random initialization method extends to about 7 s, whereas the proposed AHVC method achieves convergence within 3 s. During steady-state operation, traditional random initialization method exhibits an average convergence time of about 5 s, while the proposed AHVC method reduces this to about 3 s.

On the other hand, as shown in Fig. SA6 in Supplementary Material A, the surges of var also impact voltage stability of the PCC. The voltage curve represents voltage fluctuations of PCC when STATCOM is deactivated. For traditional methods, a voltage spike of approximately 0.025 p.u. occurs.

When STATCOM is activated to regulate the voltage at 1.08 p.u., its var output (bar chart) is referenced on the left *y*-axis. For traditional control methods, STATCOM experiences periodic 1 s var margin shortages, occasionally exceeding its limits. This prevents the backup STATCOM from being deactivated and results in low efficiency of utilization. In contrast, the proposed AHVC method effectively resolves this issue, allowing the backup STATCOM to remain in cold standby status.

This paper aims to enhance the var margin of STATCOM while limiting the data throughput. To quantify this relationship, the ratio of var margin to data throughput is defined as the average benefit-cost ratio. Additionally, min-max normalization is applied for statistical analysis to facilitate comparisons.

Secondly, Fig. 11 illustrates the troubleshooting process for an agent in the four cases of inter-agent anomalies described in Section IV. For comparison purposes, slave agent 5 is selected as an example to analyze the total var output iteration process of its subgroup in different fault scenarios. In Fig. 11, the two red dashed lines indicate the start and end time of the fault occurrence. The colors of the stacked bar chart represent the var output of subgroups 1-16 from bottom to top, respectively.

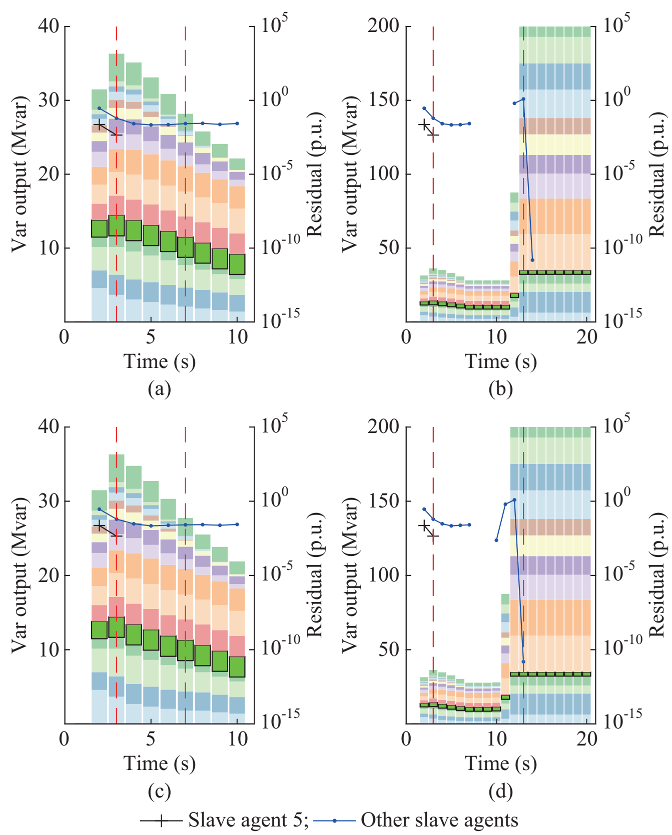

Fig. 11. Troubleshooting process for agent. (a) Case 1 or 2. (b) Case 3. (c) Case 4 (short-term). (d) Case 4 (long-term).

Additionally, the simulation demonstrates that reduced var output of STATCOM signifies improved control efficiency, highlighting the effectiveness of the proposed AHVC method. To further evaluate the impact of fault rates on control performance, a roulette wheel selection method is used to set three communication failure scenarios of 0%, 20%, and 40%, respectively. The regulation burden on STATCOM under these fault conditions is recorded in Fig. SA7 in Supplementary Material A and Table II.

Due to its asynchronous communication structure, the proposed AHVC method does not require all slave agents to complete data updates simultaneously. On one hand, it ensures the computational efficiency of slave agents with successful communication. On the other hand, it provides significant redirection time for those with communication failures.

Conversely, the distributed control method, which requires high data throughput, is more heavily impacted by communication failures. When the failure rate exceeds 40%, a standby STATCOM is necessary to maintain PCC voltage stability, and the WT voltage fluctuation range increases by 115.7%. In the mentioned tests, the proposed AHVC method does not require to activate the standby STATCOM and keeps the var margin of primary STATCOM to be above 30.7%, showcasing excellent robustness. Regarding the average benefit-cost ratio, the proposed AHVC method and distributed control method achieve comparable control performance under fault-free conditions. However, as the fault rate increases, the performance of the distributed control method declines significantly, whereas the proposed AHVC method maintains a ratio of at least 87%.

VI. Conclusion

This paper presents an AHVC method optimized under poor communication conditions in offshore wind farms. On one hand, asynchronous communication between agents enhances interference resistance and robustness. On the other hand, synchronous communication within subgroups ensures coordinated actions of WTs, preventing violations to the converter limit. Static simulation results show that the accumulative deviation of voltage control using the proposed AHVC method is 60.9%-95.6% lower than those of other methods. It significantly improves the var margin of both the STATCOM and WTs. The dynamic simulation results show that the proposed AHVC method limits voltage fluctuations of wind farm within 1.9×10^{-3} p.u. under communication failure of 0%-40%. It maintains the primary STATCOM margin and the average benefit-cost ratio above 37.8% and 88.02%, respectively. The control performance remains largely unaffected by the operation of agents under abnormal conditions. Compared with other methods, the proposed AHVC method combines the real-time responsiveness of distributed control methods with the strong resistance to interference of centralized control methods, offering significant practical utility for real-world deployment in wind farms.

References

[1] T. Zuo, Y. Zhang, K. Meng *et al.*, "Collector system topology design for offshore wind farm's repowering and expansion," *IEEE Transac-*

tions on Sustainable Energy, vol. 12, no. 2, pp. 847-859, Sept. 2020.

[2] Q. Li, Y. Zhang, T. Ji *et al*., "Volt/var control for power grids with connections of large-scale wind farms: a review," *IEEE Access*, vol. 6, pp. 26675-26692, May 2018.

[3] M. N. Naz, S. Imtiaz, M. K. L. Bhatti *et al*., "Dynamic stability improvement of decentralized wind farms by effective distribution static compensator," *Journal of Modern Power Systems and Clean Energy*, vol. 9, no. 3, pp. 516-525, May 2021.

[4] A. K. Pathak, M. P. Sharma, and M. Bundele, "A critical review of voltage and reactive power management of wind farms," *Renewable and Sustainable Energy Reviews*, vol. 51, pp. 460-471, Nov. 2015.

[5] A. Rehman, M. A. Koondhar, Z. Ali *et al*., "Critical issues of optimal reactive power compensation based on an HVAC transmission system for an offshore wind farm," *Sustainability*, vol. 15, no. 19, p. 14175, Oct. 2023.

[6] S. Jung and G. Jang, "A loss minimization method on a reactive power supply process for wind farm," *IEEE Transactions on Power Systems*, vol. 32, no. 4, pp. 3060-3068, Jul. 2017.

[7] B. Zhang, P. Hou, W. Hu *et al*., "A reactive power dispatch strategy with loss minimization for a DFIG-based wind farm," *IEEE Transactions on Sustainable Energy*, vol. 7, no. 3, pp. 914-923, Jul. 2016.

[8] H. Peng, S. Huang, P. Wang *et al*., "An online feedback-based local method for topology identification and var/volt control in radial wind farms," *IEEE Transactions on Industrial Informatics*, vol. 20, no. 3, pp. 4292-4304, Mar. 2024.

[9] T. Ding, S. Liu, W. Yuan *et al*., "A two-stage robust reactive power optimization considering uncertain wind power integration in active distribution networks," *IEEE Transactions on Sustainable Energy*, vol. 7, no. 1, pp. 301-311, Jan. 2016.

[10] J. Martínez, P. C. Kjær, P. Rodriguez *et al*., "Comparison of two voltage control strategies for a wind power plant," in *Proceedings of 2011 IEEE/PES Power Systems Conference and Exposition*, Phoenix, USA, Mar. 2011, pp. 1-9.

[11] S. Li, Y. Zhang, X. Yu *et al*., "Reactive power dispatch of DFIGs in wind farm based on multi-object optimization," *International Transactions on Electrical Energy Systems*, vol. 30, no. 3, p. 12205, Mar. 2020.

[12] Y. Zhou, Z. Li, and G. Wang, "Study on leveraging wind farms' robust reactive power range for uncertain power system reactive power optimization," *Applied Energy*, vol. 298, p. 117130, Sept. 2021.

[13] S. Huang, Q. Wu, Y. Guo *et al*., "Distributed voltage control based on ADMM for large-scale wind farm cluster connected to VSC-HVDC," *IEEE Transactions on Sustainable Energy*, vol. 11, no. 2, pp. 584-594, Apr. 2020.

[14] S. Bose, S. H. Low, T. Teeraratkul *et al*., "Equivalent relaxations of optimal power flow," *IEEE Transactions on Automatic Control*, vol. 60, no. 3, pp. 729-742, Mar. 2015.

[15] W. Jiao, Q. Wu, S. Huang *et al*., "Decentralized voltage control of wind farm based on gradient projection method," *International Journal of Electrical Power & Energy Systems*, vol. 123, p. 106308, Dec. 2020.

[16] Y. Guo, H. Gao, D. Wang *et al*., "Online optimal feedback voltage control of wind farms: decentralized and asynchronous implementations," *IEEE Transactions on Sustainable Energy*, vol. 12, no. 2, pp. 1489-1492, Jun. 2020.

[17] Y. Guo, H. Gao, and Z. Wang, "Distributed online voltage control for wind farms using generalized fast dual ascent," *IEEE Transactions on Power Systems*, vol. 35, no. 6, pp. 4505-4517, Nov. 2020.

[18] M. Wang, K. Liao, J. Yang *et al*., "Three-stage robust voltage/var optimal control of wind farms at multiple time scales," *IET Renewable Power Generation*, vol. 16, no. 3, pp. 594-606, Feb. 2022.

[19] L. Guan and J. Yao, "Dynamic coupling and cooperative control for multi-paralleled doubly fed induction generator wind farms during symmetrical low voltage ride-through in a weak grid," *Protection and Control of Modern Power Systems*, vol. 9, no. 3, pp. 112-125, May 2024.

[20] B. Li, D. Zheng, B. Li *et al*., "Analysis of low voltage ride-through capability and optimal control strategy of doubly-fed wind farms under symmetrical fault," *Protection and Control of Modern Power Systems*, vol. 8, no. 2, pp. 1-15, Apr. 2023.

[21] Z. Jiang and Y. Liu, "Low-voltage ride-through remote testing method for offshore wind turbines," *IEEE Transactions on Instrumentation and Measurement*, vol. 69, no. 6, pp. 2905-2913, Jun. 2020.

[22] P. Liu, Z. Li, Y. Zhuo *et al*., "Design of wind turbine dynamic trip-off risk alarming mechanism for large-scale wind farms," *IEEE Transactions on Sustainable Energy*, vol. 8, no. 4, pp. 1668-1678, Oct. 2017.

[23] J. Zhang, Z. Chen, C. He *et al*., "Data-driven-based optimization for power system var-voltage sequential control," *IEEE Transactions on Industrial Informatics*, vol. 15, no. 4, pp. 2136-2145, Jul. 2018.

[24] S. Boyd, N. Parikh, E. Chu *et al*., *Distributed Optimization and Statistical Learning via the Alternating Direction Method of Multipliers*. Hanover: Now Foundations and Trends, 2011.

[25] C. Sun, "Rank-constrained optimization: algorithms and applications," Ph.D. dissertation, The Ohio State University, Columbus, USA, 2018.

[26] L. Li, X. Wang, and G. Wang, "Alternating direction method of multipliers for separable convex optimization of real functions in complex variables," *Mathematical Problems in Engineering*, vol. 2015, p. 104531, Dec. 2015

[27] P. Wang, Q. Wu, S. Huang *et al*., "ADMM-based distributed active and reactive power control for regional AC power grid with wind farms," *Journal of Modern Power Systems and Clean Energy*, vol. 10, no. 3, pp. 588-596, May 2022.

[28] D. K. Molzahn, F. Dörfler, H. Sandberg *et al*., "A survey of distributed optimization and control algorithms for electric power systems," *IEEE Transactions on Smart Grid*, vol. 8, no. 6, pp. 2941-2962, Nov. 2017.

[29] W. Deng, M. J. Lai, Z. Peng *et al*., "Parallel multi-block ADMM with $o(1/k)$ convergence," *Journal of Scientific Computing*, vol. 71, no. 2, pp. 712-736, May. 2017.

[30] D. Gebbran, S. Mhanna, A. C. Chapman *et al*., "Multiperiod DER coordination using ADMM-based three-block distributed AC optimal power flow considering inverter volt-var control," *IEEE Transactions on Smart Grid*, vol. 14, no. 4, pp. 2874-2889, Dec. 2022.

[31] M. Li, D. Sun, and K. C. Toh, "A convergent 3-block semi-proximal ADMM for convex minimization problems with one strongly convex block," *Asia-Pacific Journal of Operational Research*, vol. 32, no. 4, p. 1550024, Aug. 2015.

[32] M. Nakao and S. Sugiura, "Spectrally efficient frequency division multiplexing with index-modulated non-orthogonal subcarriers," *IEEE Wireless Communications Letters*, vol. 8, no. 1, pp. 233-236, Feb. 2019.

[33] J. Yang, N. Zhang, C. Kang *et al*., "A state-independent linear power flow model with accurate estimation of voltage magnitude," *IEEE Transactions on Power Systems*, vol. 32, no. 5, pp. 3607-3617, Sept. 2017.

Yongjun Zhang received the B.Sc. and Ph.D. degrees in electrical engineering and its automation from South China University of Technology, Guangzhou, China, in 1995 and 2004, respectively. He is currently a Professor with the School of Electric Power, South China University of Technology. His research interests include reactive power optimization of power system, optimal control of active distribution network, and high-voltage direct current.

Kanghua Zhong received the B.E. degree in electrical engineering and its automation from Shanghai University of Electric Power, Shanghai, China, in 2020. He is currently pursuing the Ph.D. degree in electrical engineering at South China University of Technology, Guangzhou, China. His research interests include automatic volt/var optimal control, offshore wind power grid-connected control, analysis and control of AC and DC hybrid power system, and distributed optimization.

Yingqi Yi received the Ph.D. degree in electrical engineering from South China University of Technology, Guangzhou, China, in 2024. Currently, he is a Postdoctoral Researcher with the School of Electric Power, South China University of Technology. His research interests include big data analysis and application in distribution system, and virtual power plant.

Yang Liu received the B.E. and Ph.D. degrees in electrical engineering from South China University of Technology, Guangzhou, China, in 2012 and 2017, respectively. He is currently an Associate Professor with the School of Electric Power, South China University of Technology. His research interests include power system stability analysis and control, control of wind power generation system, and nonlinear control theory.